ALES+: Adapting a homogenous ocean retracker for satellite altimetry to sea ice leads, coastal and inland waters.

Marcello Passaro[a,], Stine Kildegaard Rose[b], Ole B. Andersen[b], Eva Boergens[a], Francisco M. Calafat[c], Denise Dettmering[a], Jérôme Benveniste[d]

[a]*Deutsches Geodätisches Forschungsinstitut der Technischen Universität München, Arcisstraße 21, 80333 Munich, Germany. Contacts: marcello.passaro@tum.de, +49 (89) 23031-1214*
[b]*DTU-Space, National Space Institute, Kgs.Lyngby, Denmark*
[c]*National Oceanography Centre Liverpool, Liverpool, United Kingdom*
[d]*European Space Research Institute (ESRIN), European Space Agency, Frascati, Italy*

Abstract

Water level from sea ice-covered oceans is particularly challenging to retrieve with satellite radar altimeters due to the different shapes assumed by the returned signal compared with the standard open ocean waveforms. Valid measurements are scarce in large areas of the Arctic and Antarctic Oceans, because sea level can only be estimated in the openings in the sea ice (leads and polynyas). Similar signal-related problems affect also measurements in coastal and inland waters.

This study presents a fitting (also called retracking) strategy (ALES+) based on a subwaveform retracker that is able to adapt the fitting of the signal depending on the sea state and on the slope of its trailing edge. The algorithm modifies the existing Adaptive Leading Edge Subwaveform retracker originally designed for coastal waters, and is applied to Envisat and ERS-2 missions.

The validation in a test area of the Arctic Ocean demonstrates that the presented strategy is more precise than the dedicated ocean and sea ice retrackers available in the mission products. It decreases the retracking open ocean noise by over 1 cm with respect to the standard ocean retracker and is more precise by over 1 cm with respect to the standard sea ice retracker used for fitting specular echoes. Compared to an existing open ocean altimetry dataset, the presented strategy increases the number of sea level retrievals in the sea ice-covered area and the correlation with a local tide gauge. Further tests against in-situ data show that also the quality of coastal retrievals increases compared to

**This is the accepted version of the manuscript identified as https://doi.org/10.1016/j.rse.2018.02.074 and available at https://www.sciencedirect.com/science/article/pii/S0034425718300920

the standard ocean product in the last 6 km within the coast.

ALES+ improves the sea level determination at high latitudes and is adapted to fit reflections from any water surface. If used in the open ocean and in the coastal zone, it improves the current official products based on ocean retrackers. First results in the inland waters show that the correlation between water heights from ALES+ and from in-situ measurement is always over 0.95.

Keywords: Satellite Altimetry, retracking, subwaveform retracker, validation, tide gauge, Leads, Arctic Ocean, ALES;

1. Introduction

Sea level is an Essential Climate Variable (ECV) regarded as one of the main indicators of climate variability (Cazenave et al., 2014). For more than 25 years, traditional measurements obtained by means of in-situ pressure gauges have been supported by the repeated global remotely sensed estimations from the radar signals registered onboard satellite altimeters. This has lead to significant advancements in our knowledge of the seasonal and interannual sea level fluctuations (Vinogradov & Ponte, 2010; Ablain et al., 2016), of the regional distribution of trends in a changing climate (Palanisamy et al., 2015) and of the mid to large scales of geostrophic circulation (Pascual et al., 2006).

The basic concept of this remote sensing technique considers the sea surface height (SSH) as the difference between the height of the satellite referenced to the earth ellipsoid and the distance (range) between the satellite centre of mass and the mean reflecting surface. The SSH has then to be corrected for instrumental, atmospheric and geophysical effects. For a full description of the corrections the reader is referred to Fu & Cazenave (2001). The progress of satellite altimetry has been fostered by the developments in orbit determination (Rudenko et al., 2014), in the corrections (Handoko et al., 2017) and in the range retrieval, based on the fitting of a functional form to the received signal in a procedure called retracking (Cipollini et al., 2017).

The processing of the echoes sent by pulse-limited radar altimeters (i.e. every radar altimeter before the launch of CryoSat-2 in April 2010 and, more recently, Sentinel-3A) is well known in the open ocean, where the shape of the received signal resembles the Brown-Hayne (BH) model (Brown, 1977; Hayne, 1980) perturbed by Rayleigh noise (Quartly et al., 2001), characterised by a steep leading edge and a slowly decaying trailing edge.

Departures of the received signal (also called ’waveform’, a sampled time series whose resolution cell is called ’gate’) from the BH shape are instead found in the presence of sea ice and in the proximity of land (i.e. both in coastal and inland waters) (Boergens et al., 2016; Laxon, 1994b). The common feature is the presence of the so-called ’bright targets’ or ’hyperbolic targets’: points with a higher backscatter coefficient that perturb the expected shape travelling along the trailing edge as they appear in the illuminated area, eventually constituting the main leading edge.

These retracking issues, together with the degradation of some corrections in the same areas, have been a major impediment in expanding our knowledge of sea level variability in the coastal ocean and in the Arctic Ocean. These are regions of primary importance, since a growing number of people and infrastructures are located at the coast (Neumann et al., 2015) and since changes in the Arctic Ocean dynamics significantly affect the global climate (Marshall et al., 2014).

This study is motivated by the need of increasing the quality and the quantity of sea level retrievals in the Arctic Ocean. It focuses on a retracking procedure that is able to retrieve the ranges of pulse-limited radar altimeters reflected from the leads (water apertures in sea ice) while improving the retracking in open and coastal ocean as well. Given the similarities of the problem, we aim also at demonstrating the validity of this strategy for the retrieval of water level in inland waters. The result is the definition of a single algorithm that is able to adapt the estimation to any kind of water returns.

Here, our efforts are aimed at improving the times series for 1995-2010 by fitting the signals from the altimeters on two European Space Agency (ESA) missions: ERS-2 and Envisat, which have occupied the same ground tracks of a 35-day repeat cycle between latitudes 82° S and 82° N.

Previous and on-going studies share the objective of improving the quality of satellite altimetry at high latitudes. Giles et al. (2007) applied a dedicated empirical functional form to lead waveforms, separating the typical peaky shape into a Gaussian and an exponential function. For the open water points though, they used the standard product, which adopts the BH fitting. The use of heterogenous retrackers leads to a significant bias, which was quantified in 15±11 cm. Two different retrackers for ocean and leads and a consequent bias adjustment were also the choice of Peacock & Laxon (2004). More recently, Cheng et al. (2015) edited the Envisat data from the Radar Altimetry

Database System (RADS) without applying a specific retracker, while Poisson et al. (2017) (personal communication) are also aiming at a homogenous retracking strategy, as this paper, by using the modified BH proposed by Jackson et al. (1992), in which the peakiness of the waveform is modelled by a surface roughness parameter.

Our starting point is the Adaptive Leading Edge Subwaveform (ALES) retracker by Passaro et al. (2014), which is based on a BH fitting of a portion of the echo in order to avoid bright targets on the trailing edge of the waveforms. The ALES-reprocessed altimetry data have already been validated against in-situ measurements from tide gauges (TGs) and used for coastal sea level variability studies (Passaro et al., 2015a, 2016). The potential for the application to peaky echoes was already identified in a paper by Passaro et al. (2015b), where ALES was applied on the tidal flats in the German Bight, whose still waters produce returns analogous to lead echoes. Here, we develop a new version of the algorithm (ALES+) to improve the fitting of the peaky waveforms and abate the noise in the open ocean compared to the standard processing.

In the framework of the ESA Sea Level Climate Change Initiative (SL CCI), ALES+ will be the retracker of choice for Envisat and ERS-2 missions in the DTU/TUM high latitude sea level product (Rose et al., in preparation). Therefore, the main part of this paper is dedicated to the description and validation of the ALES+ solution in a test zone of the Arctic Ocean. We also evaluate the performances at the coast and in the inland waters, in order to exploit ALES+ as a homogenous retracker solution for any kind of water surfaces.

The dataset and the areas of study are defined in Section 2; The ALES+ procedure and the methodologies followed to identify leads among the sea ice are described in Section 3; validation and discussion follow in Section 4, while Section 5 derives the conclusions.

2. Areas of Study and Datasets

2.1. Areas of Study

As a main area of study the surroundings of the Svalbard Islands (the Svalbard test area, latitude limits: $78 - 82°N$, longitude limits: $0 - 20°E$) are chosen, in order to validate ALES+ in the sea ice and in the open ocean. This geographical box presents both constant open water and sea ice. The presence of a TG, which is very rare at such latitudes, also allows a validation in areas that are seasonally covered by sea ice. Figure

1 (a) shows the minimum (September 2007) and maximum (February 1998) extent of the sea ice during the period considered in this study, provided by the Sea Ice Index Data and Image Archive at NSIDC (Fetterer et al., 2016) and is given as a monthly sea ice extent polygon. Also the TG Ny Ålesund used in the validation is shown in Figure 1 (a).

To validate ALES+ as a coastal retracker, the coastal waters of a region in the North-East Atlantic Ocean within 70 km of the coast are considered, due to the availability of local TG data with high temporal resolution. Figure 1 (b) displays the TGs used in the study and highlights in red the analysed segments of the altimetry tracks.

Finally, the Mekong River is taken as example of an inland water application in order to allow the comparison with previous studies that exploit the synergy between altimetry and in-situ stations, which are shown in Figure 1 (c).

2.2. Satellite Altimetry Data

The waveforms and all the additional information needed to apply the ALES+ algorithm are taken from the ESA Sensor Geophysical Data Records (SGDR) of ERS-2 REAPER (Femenias et al., 2014) and Envisat version 2.1. For Envisat the entire duration of the phase 2 (May 2002 - October 2010) is considered; for ERS-2 the REAPER data cover the period from September 1995 to July 2003. The RADS altimetry database ($http://rads.tudelft.nl/$) with its default settings is used to provide an alternative sea level anomaly (SLA, see Section 3.3) product for comparisons..

2.3. In-situ Data

In the sea ice region Revised Local Reference (RLR) TG data of the Ny Ålesund station are downloaded as monthly averages from the Permanent Service for Mean Sea Level (PSMSL) at http://www.psmsl.org/data/obtaining/stations/1421.php. In the coastal region TG records were obtained from the UK National Tide Gauge Network archives at the British Oceanographic Data Centre (BODC) and the University of Hawaii Sea Level Center (UHSLC). The temporal resolution of the sea level data is 15 minutes for records stored at the BODC and 1 hour for those stored at the UHSLC. Here, we use a set of 10 TGs with nearly continuous records of sea level over the period 1995-2010, which have been visually inspected for shifts and outliers. In the Mekong river, telemetric gauge data is provided by the Mekong River Commission (MRC, http://ffw.mrcmekong.org/). The latter has a daily resolution, but no absolute height reference.

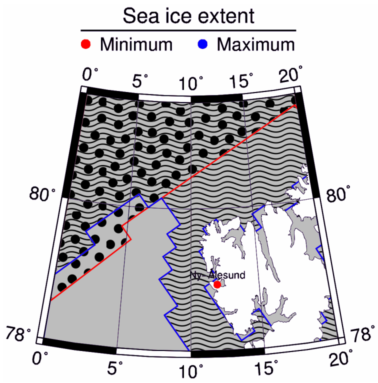

(a)

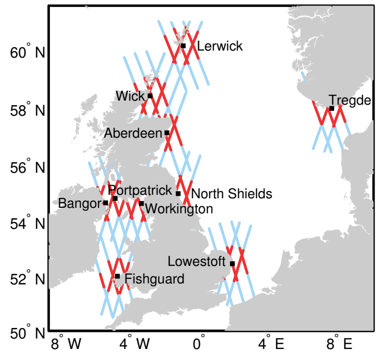

(b)

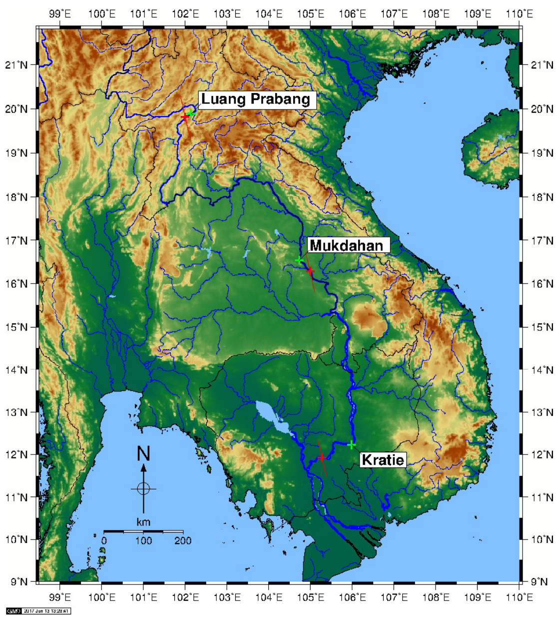

(c)

Figure 1: (a) The Svalbard test area in the Arctic Ocean. The dotted area with red border is the minimum sea ice cover, while the wavy area with blue border is the maximum. The red dot indicates the location of the Ny Ålesund TG used for validation. (b and c) Location of the TGs used for coastal and inland waters validation and (red) along-track extension of nominal Envisat and ERS-2 tracks used for comparison with in-situ data.

This kind of in-situ data are widely used by the Scientific Community as validation means. All types of TG (acoustic, pressure, float, and radar) can measure sea-level variations with an accuracy of at least 1 cm (see the IOC Manual on Sea Level at $http://www.psmsl.org/train\_and\_info/training/manuals$), which is significantly better than the accuracy achieved by altimeters. Telemetric river monitoring system is considered to reach a mm accuracy (see $http://www.radio-data-networks.com/products/flooding/radar-based-river-level-monitoring-telemetry/$)

3. Methodology

3.1. ALES+ Retracker

3.1.1. The Brown-Hayne model

ALES+ inherits the functional form used to fit the waveforms from the BH model. In order to clarify the terminology in use, we report here the corresponding Equations. The return power V_m is

$$V_m(t) = a_\xi P_u \frac{[1 + \mathrm{erf}(u)]}{2} \exp(-v) + T_n \tag{1}$$

where

$$\mathrm{erf}(x) = 2\frac{1}{\sqrt{\pi}} \int_0^x e^{-t^2} dt \qquad a_\xi = \exp\left(\frac{-4\sin^2\xi}{\gamma}\right) \qquad \gamma = \sin^2(\theta_0)\frac{1}{2 \cdot \ln(2)} \tag{2}$$

$$u = \frac{t - \tau - c_\xi \sigma_c^2}{\sqrt{2}\sigma_c} \qquad v = c_\xi\left(t - \tau - \frac{1}{2}c_\xi \sigma_c^2\right) \tag{3}$$

$$\sigma_c^2 = \sigma_p^2 + \sigma_s^2 \qquad \sigma_s = \frac{SWH}{2c} \tag{4}$$

$$c_\xi = b_\xi a \qquad a = \frac{4c}{\gamma h\left(1 + \frac{h}{R_e}\right)} \qquad b_\xi = \cos(2\xi) - \frac{\sin^2(2\xi)}{\gamma} \tag{5}$$

where c is the speed of light, h the satellite altitude, R_e the Earth radius, ξ the off-nadir mispointing angle, θ_0 the antenna beam width, τ the Epoch with respect to the nominal tracking reference point (linked to the range), σ_c the rise time of the leading edge (depending on a term σ_s linked to the Significant Wave Height (SWH) and on the width of the radar point target response σ_p), P_u the amplitude of the signal (linked to the backscatter coefficient σ_0) and T_n the thermal noise level.

The variables that can alter the slope of the trailing edge in BH are all contained in the term c_ξ. It is important to note that c_ξ has also a small effect on u via the term $c_\xi \sigma_c^2$. This means that changes in c_ξ also slightly affect the position of the retracking point τ along the leading edge. An approach to fit the trailing edge slope was also attempted in other studies, such as in the empirical 5-parameter model by Deng & Featherstone (2006), in which nevertheless a change in the parameter related to the slope of the trailing edge would not cause any change in the location of the retracking point on the leading edge.

In Equations 1-5, the trailing edge slope variability is constrained by the fact that θ_0 is given and the variations of ξ are slow and must be smaller than 0.3° (Dorandeu et al., 2004). While these constraints correctly model a typical open ocean response, they prevent the fitting of peakier waveforms. Therefore, in order to be able to fit waveforms with a steep trailing edge slope, ALES+ preliminary estimates c_ξ. The steps followed by ALES+ are the following:

1. Detection of the leading edge
2. Choice of c_ξ
3. First retracking of a subwaveform restricted to the leading edge, i.e. first estimation of the SWH
4. Extension of the subwaveform using a linear relationship between width of the subwaveform and first estimation of the SWH
5. Second retracking of the extended subwaveform, i.e. precise determination of τ, SWH and P_u

Steps 1 and 2 are described respectively in Section 3.1.2 and Section 3.1.3. Steps 3 to 5 are unchanged compared to the ALES retracker (Passaro et al., 2014) and they are recalled in Section 3.1.4. A flow diagram of the main steps followed by ALES+ to retrack each waveform is shown in Figure 2.

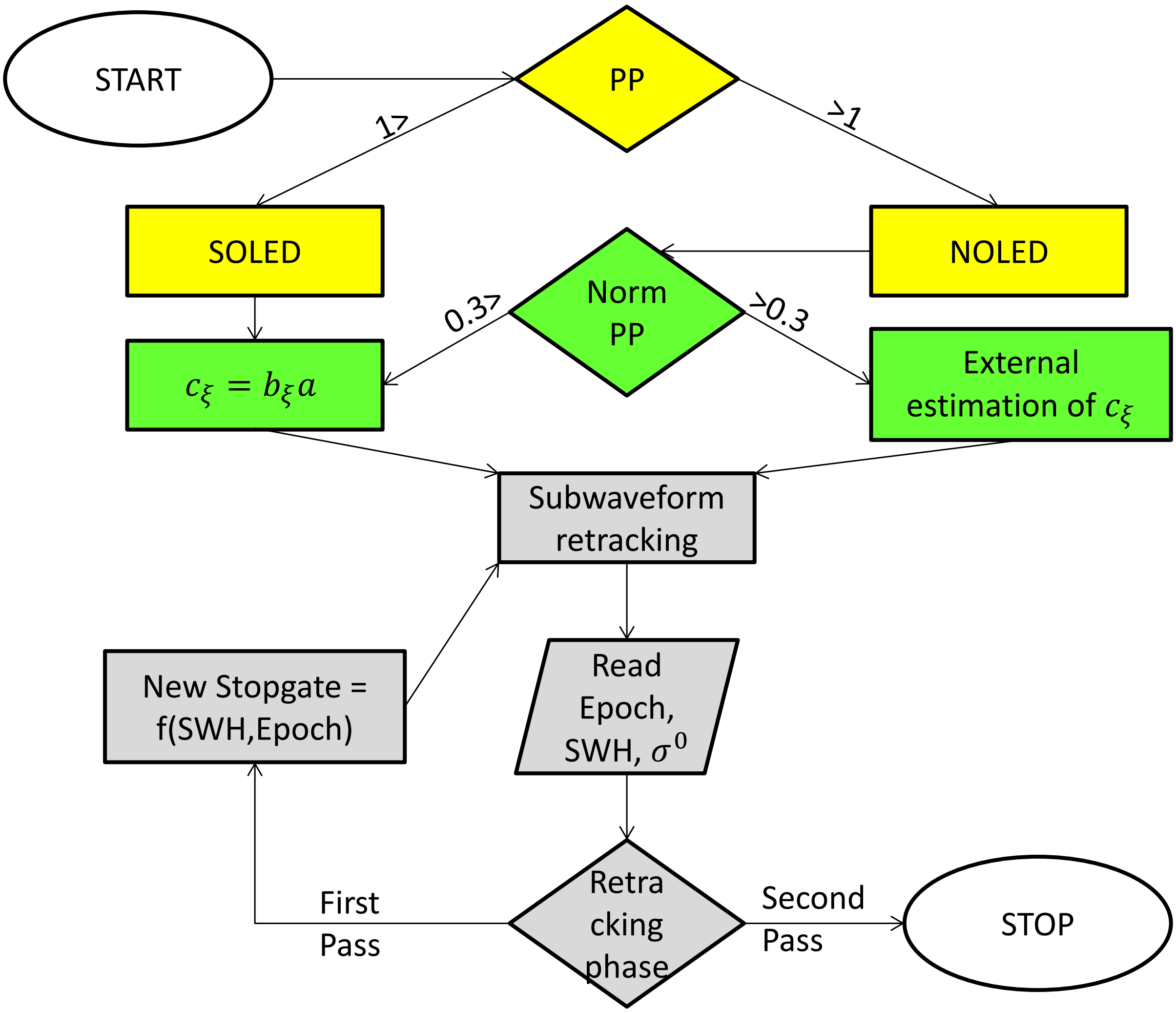

Figure 2: Flow diagram of ALES+ retracking procedure for each waveform. PP stands for Pulse Peakiness, Norm PP for Pulse Peakiness computed on the normalised waveforms. SOLED and NOLED are the leading edge detection procedures for standard and non-standard ocean waveforms described in Section 3.1.2. The steps highlighted in green are described in Section 3.1.3 and the ones in grey, analogous to ALES in Passaro et al. (2014), are recalled in Section 3.1.4.

3.1.2. Leading edge detection

Since ALES+ is based on the selection of a subwaveform, it is essential that the leading edge, containing the information on the range between satellite and reflecting surface, is correctly detected in all cases. Lead waveforms and ocean/coastal waveforms are characterised in this respect in two different ways: in the first case, the lead return (if at nadir) clearly dominates any other return, but the decay of the trailing edge is extremely quick; in the latter, the leading edge is better characterised, but spurious strong returns can precede (if from icebergs, ships, or targets at a higher height than the water level) or follow (if from areas of the footprint characterised by different backscatter characteristics) the main leading edge, whose trailing edge decreases very slowly.

To distinguish between the two cases, a Pulse Peakiness (PP) index is computed in ALES+ following the formula in Peacock & Laxon (2004). The order of magnitude of PP ranges from 10^{-1} for waveforms in which the peak power is comparable to the average backscatter in the other waveform gates, to over 10^{1} for echoes dominated by a strong specular reflector. Waveforms with PP<1 are sent to the standard ocean leading edge detection (SOLED) procedure, the others are sent to the non-standard ocean leading edge detection procedure (NOLED). This is not a physical classification aimed at detecting leads, but only a way to aid the correct detection of the leading edge; moreover, the retracking (steps 3-5 in Section 3.1.1) remains the same in both cases.

Non-standard ocean waveforms are in our case not only the leads (peaky waveforms), but any waveform whose trailing edge decay is more pronounced than in the standard ocean return. We do not exclude the waveforms coming from sea ice, since these are excluded in the post-processing by the classification of Section 3.2. The aim is therefore different from Peacok and Laxon (2004), in which a strict classification is needed in order to send each kind of waveform to a different retracker and to avoid the detection of false leads, which would cause inconsistencies in the sea level retrieval.

The steps followed by NOLED are the following:

1. The waveform is normalised with normalisation factor N, where N = 1.3 * median(waveform)
2. The temptative starting point of the leading edge, defined as startgate, is assigned to the first gate higher than 0.01 normalised power units compared to the previous gate
3. If any of the subsequent 4 gates after the selected startgate have a normalised power below 0.1 units, the algorithm goes back to step 2 and a new startgate is found
4. The end of the leading edge (stopgate) is fixed at the first gate in which the derivative changes sign (i.e. the signal start decreasing and the trailing edge begins), if the change of sign is kept for the following 3 gates.

The steps followed by SOLED are the following:

1. The waveform is normalised with normalisation factor N, where N = max(waveform)

2. The stopgate is the maximum value of the normalised waveform
3. Going backwards from stopgate, the startgate is the first gate in which the derivative is lower than 0.001 units

N=1.3*median(waveform) was chosen empirically as a reference power whose value is close to the maximum of the leading edge also in case of high trailing edge noise. Note that for NOLED waveforms the maximum of the leading edge does not necessarily correspond to the maximum power registered in the waveform, since it may come from spurious coastal reflections and/or noise in the trailing edge.

3.1.3. Choice of c_ξ

The non-standard ocean waveforms undergo a further preliminary step: c_ξ is estimated externally. Beforehand, a further check on the PP recomputed on the normalised waveform (Norm PP >0.3) is computed in order to avoid, where possible, the estimation of c_ξ in the presence of other peaks in the trailing edge. Norm PP is useful because by using a normalised waveform it is easier to set up a threshold for all peaky waveforms regardless of their maximum backscatter power, which greatly differ between specular reflections (Passaro et al., 2017). The threshold was determined by empirical observation of waveforms, of which Figure 3 provides an example.

In the external estimation, the full waveform is fitted using a simplified BH model up to Equations 4, having 4 unknowns: τ,σ_c,P_u, c_ξ. From this result, only c_ξ is kept and used as an input in the remaining steps of the ALES+ algorithm.

If Norm PP <0.3, c_ξ is computed from Equations 5.

c_ξ can be therefore estimated for all the waveforms that successfully pass through SOLED and if Norm PP >0.3, i.e. all the peaky waveforms in which one clear leading edge can be identified. Since the estimation of c_ξ is suitable for peaky waveforms, irregular waveforms where no leading edge is identifiable cannot be correctly fitted by ALES+. Figure 4 shows the estimations of c_ξ for cycle 35 of Envisat (February-March 2005). The areas where c_ξ is estimated are all located in the sea-ice-covered region.

3.1.4. Subwaveform retracking

Steps 3 to 5 are analogous to the ALES retracker. In step 3, a first subwaveform from startgate to stopgate is fitted with the BH model having τ,σ_c,P_u as unknowns.

The SWH derived from σ_c and τ are used in step 4 to compute the new stopgate using the following linear relationship:

$$\text{Stopgate} = \text{Ceiling}(\text{ Tracking point } + \ 2.4263 \ + \ 4.1759 \times \text{SWH }) \tag{6}$$

for Envisat and:

$$\text{Stopgate} = \text{Ceiling}(\text{ Tracking point } + \ 3.1684 \ + \ 2.3203 \times \text{SWH }) \tag{7}$$

for ERS-2. The Tracking point is the gate corresponding to the estimated Epoch τ.

Finally, in step 5 a new fitting is performed using a subwaveform up to the new stopgate and the final estimations of τ,σ_c and P_u are obtained. Note that in every fitting, the subwaveform is oversampled by means of the Akima interpolation by Akima (1970) in order to increase the redundancy of the information across the leading edge as described in Passaro et al. (2015b); in ALES+, the waveforms are oversampled by a factor of 8 for both Envisat and ERS-2.

Figure 5 shows three examples of ALES+ waveform fitting for three different trailing edge slope conditions typical of open ocean, coast and leads. A black vertical line highlights the location of the retracking point estimated by ALES+. In the lead case (Figure 5c), it is evident how the retracking point (Epoch) is not located at the mid-point of the visible leading edge, since the retracking point τ and c_ξ are present both in the exponential term v and in the argument of the error function u as described in Section 3.1.1. This effect is not simply empirical, but is related to the mean square slope (MSS) of the sea surface, as shown in Jackson et al. (1992). In the latter, the so-called trailing edge parameter, which has an effect on the retracking point as well, depends explicitly on the MSS and hence on the surface roughness. Indeed, using the mid-point of the 'visible' leading edge as the retracking point of any peaky waveform has no physical meaning, because the waveform, i.e. a discrete time series, is in this case highly undersampled: the information on the position of the true maximum power and consequently the location of the true mid-point of the leading edge cannot be retrieved. ALES+ cannot create new information and solve the problem of the undersampled leading-edge, but it can perform a consistent guess of τ given c_ξ, using an existing waveform model and adapting it to a more general case.

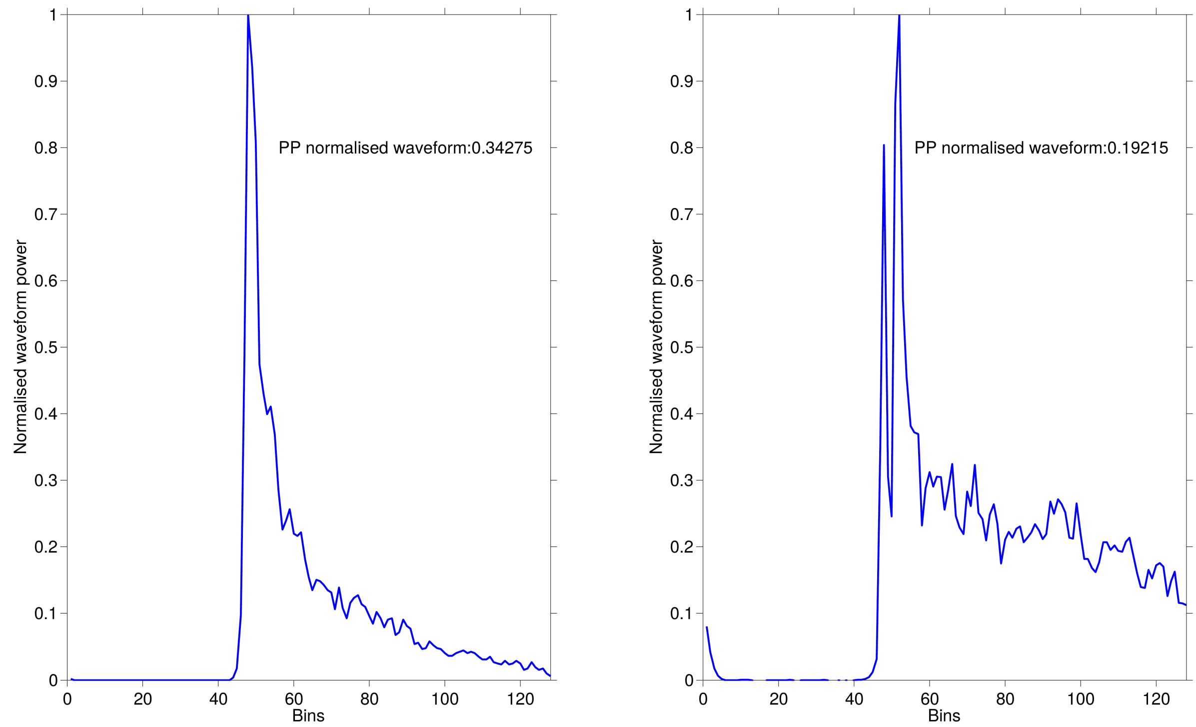

Figure 3: Normalised waveforms and their pulse peakiness (Norm PP). Left: a peaky waveform in which c_ξ can be estimated by ALES+; Right: a waveform with a peak following the trailing edge.

3.1.5. Sea State Bias recomputation

The Sea State Bias (SSB) is among the time-variable corrections that are applied to SSH estimates from satellite altimetry. SSB is linked with both the signal processing of the radar echo and the interaction between the latter and the waves. Given the theoretical complexity and the different sources of SSB, the accepted procedure to derive an SSB correction is to infer an empirical relationship between the height error due to SSB, and the SWH and wind speed (derived from σ^0) estimated from the retracking of each altimetry mission. Sandwell & Smith (2015) have studied the relationship between the parameters estimated by the retracking algorithms (range, SWH and σ^0) and have found significant correlated errors. In the same study, they argue that correlated errors in the retrackers explain a significant part of the SSB. It is therefore fundamental to correct the ranges for the SSB corresponding to SWH and σ^0 values estimated by the same retracker.

The SSB applied to the ALES+ data is obtained by bilinear interpolations from a look-up table in which this correction is a function of SWH and Wind Speed (Labroue, 2007). The look-up table could be obtained from the SGDR data by tabulating the values

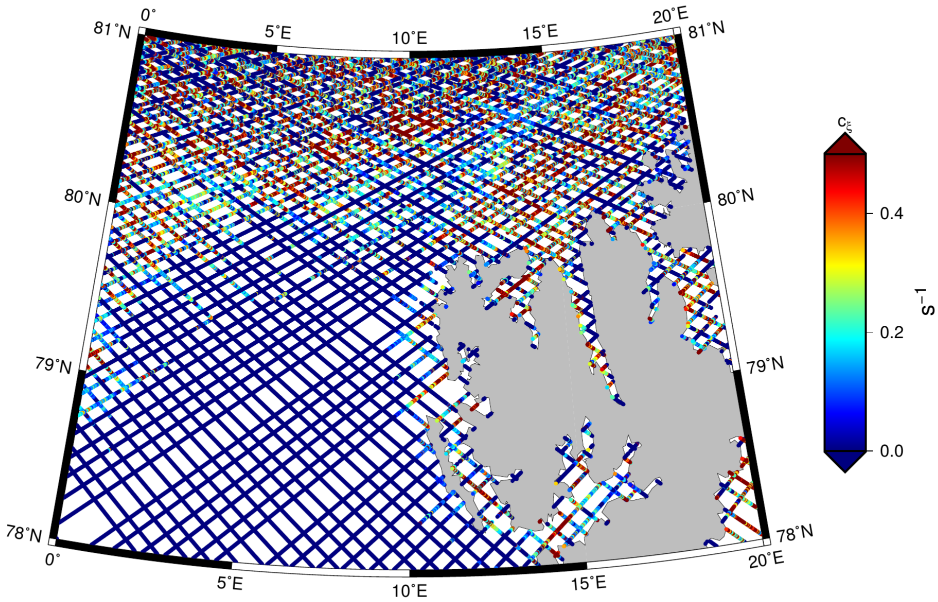

Figure 4: Estimations of c_ξ for cycle 35 of Envisat. In the plot, c_ξ is set to 0 for NOLED waveforms and for waveforms in which Norm PP <0.3, because c_ξ is in these cases not estimated.

assumed by the given SSB correction for each value of SWH and Wind. In order to be more accurate, the authors have obtained the look-up table with permission from Collecte Localisation Satellite (CLS). When performing the bilinear interpolations, SWH and σ^0 obtained from ALES+ were used. σ^0 was converted to wind speed using the algorithm described in Abdalla (2012). This follows the procedure applied and validated against in-situ data for ALES Envisat in Gómez-Enri et al. (2016). For ERS-2, we use the same look-up Table as for Envisat mission, since the one used in the REAPER product has not been published (Gilbert et al., 2014).

3.2. Waveform classification

To allow the validation of the retracking strategy in the sea ice region, lead and open ocean waveforms need to be isolated by means of a classification algorithm. For our purposes, given that sea ice waveforms can be hard to distinguish from open ocean returns (Drinkwater, 1991; Laxon, 1994a), we first separate the ice-covered region from the open ocean using the daily ice concentration grids from the Global Sea Ice Concentration

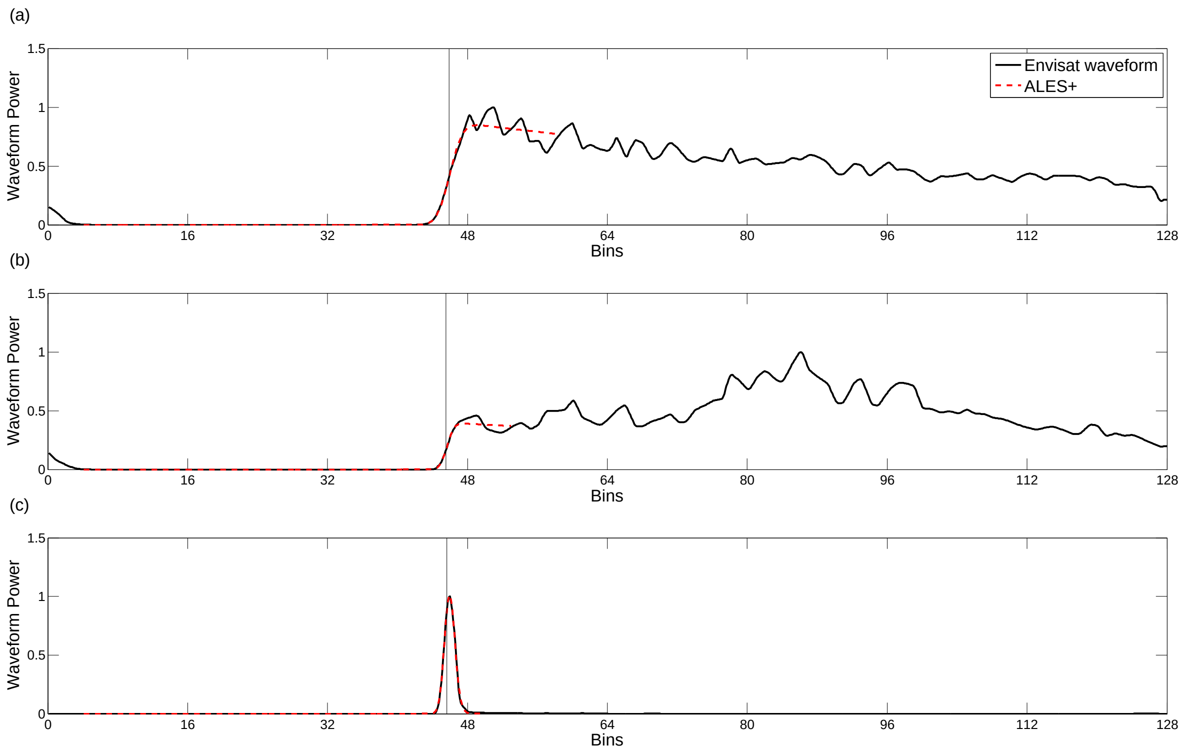

Figure 5: Examples of ALES+ waveform fitting for three different trailing edge slope conditions typical of open ocean (a), coast (b) and leads (c). A black vertical line highlights the location of the retracking point estimated by ALES+.

Climate Data Records 1978-2015 (v1.2, 2015) of the Norwegian and Danish Meteorological Institutes (available online from EUMETSAT Ocean and Sea Ice Satellite Application Facility http://osisaf.met.no). The sea ice area is defined by all the points in the grid with a sea ice concentration over 15% (Fetterer et al., 2016).

In this study, the following classification criteria are used for both Envisat and ERS-2:

- The samples within the sea ice area characterised by PP>20 and σ_c <3 ns are classified as leads;
- The samples outside the sea ice area characterised by PP<1.5 and σ^0 <15 dB are classified as open water

Any other point is either classified as unknown or as sea ice and is therefore not considered in our analysis. The criterion on σ^0 is applied to remove spurious data near the ice edge and in the ice pack (Chelton & McCabe, 1985). Additional discussion and validation of the classification method will be provided in Rose et al. (in preparation).

3.3. Corrections applied to the range

While the retracking technique at the centre of this investigation influence the range and the SSB, as mentioned in the introduction other corrections are needed in order to obtain a sea level that is comparable to external sources for validation. In particular, we define the SSH as follows:

$$\text{SSH} = \text{Orbit altitude} - \text{Corrected Range} - (\text{Solid Earth Tide} + \text{Load Tide} + \text{Ocean Tide}) \tag{8}$$

where

$$\begin{aligned}\text{Corrected Range} = &\text{Range} + \text{Dry tropospheric correction} + \text{Wet Tropospheric Correction} + \\ &+ \text{Sea State Bias} + \text{Ionospheric correction}\end{aligned} \tag{9}$$

Note that the correction that eliminates the static and dynamic response of the sea level to the atmospheric wind and pressure forcing (often called Dynamic Atmosphere Correction) is not applied, since the water level measured by pressure gauges used for validation is also subjected to these factors.

We use the corrections for the wet and dry troposphere and for the ionosphere from the models available in the SGDR. The SSB is recomputed for ALES+ as previously described. The sea level is also corrected for tides: the FES2014 model is used in the Svalbard test area, given the improvements brought by the model in the Arctic region (Carrere et al., 2015); the Empirical Ocean Tidal model EOT2011a (Savcenko & Bosch, 2012) is used in the coastal validation, since it has scored best in a recent validation effort against coastal TGs (Stammer et al., 2014). Finally, the Sea Level Anomaly (SLA), i.e. the variation of the SSH with respect to a local mean, is obtained by subtracting the Mean Sea Surface model DTU15 to the SSH (Andersen et al., 2016).

4. Validation and discussion

4.1. Svalbard test area

4.1.1. Comparison among retrackers

The first index that proves the quality of the retracking is the fitting error on the leading edge. The fitting error is a measure of how close the fitted waveform is to the real signal and corresponds to the normalised square root of the difference between the modelled waveform and the real signal along the leading edge. It has already been used in Passaro et al. (2015a) for outliers detection. In Figure 6, the histogram of the fitting error for the waveforms classified as leads is compared to the one for the open ocean waveforms with low SWH, whose leading edge is therefore more similar to the peaky case. The fitting error of lead waveforms is in the vast majority of instances lower than for the low-SWH ocean case, which proves the capability of ALES+ to fit the leading edge of all the peaky waveforms. The statistics for ERS-2 are slightly worse than for Envisat: this can be attributed to the fact that the original ERS-2 data are defined on half the number of gates (64) compared to Envisat (128).

Firstly, we compare our retracked data with the SGDR output in the sea ice domain. In particular, concerning SGDR we consider both the ocean retracker and the sea ice retracker, which was specifically designed for the fitting of specular waveforms by Laxon (1994a) and included in the official ESA products from Envisat and ERS-2. This retracker was used to estimate sea level from leads by Peacock & Laxon (2004). Given the absence of network of high-resolution in-situ data at such latitudes, we validate the retrackers following the procedure of Deng & Featherstone (2006) by means of an independently surveyed reference . We use GOCO5s, the latest release of the GOCOs geoid model, which is independent from altimetry, being based exclusively on satellite gravimetry data (Pail et al., 2010), although as such it is not able to observe the shorter wavelengths (below 100 km) detected by the altimeter. The GOCO5s geoid height are interpolated to the altimetry tracks in the whole area and the differences between SSH and geoid height are computed. These differences of course include the mean dynamic topography and the uncertainties in the corrections to the altimetry data. Nevertheless what matters for our analysis are the differences among the retrackers and the corrections do not have an influence, since exactly the same corrections are applied to every dataset. In order to make our results independent of the performances of the waveform classification, we compute the differences for any point with PP>1 and we only keep the additional criteria of σ_c <3 ns, to be sure that we are dealing with peaky echoes. After removing outliers (absolute value of SLA above 2 m), the Median Absolute Deviation (MAD) of the differences is computed for every cycle and the average values are shown in Table 1. For both missions ALES+ is the best performing dataset, improving not only the

Table 1: Median Absolute Deviation between GOCO5s geoid heights and SSH data retracked with ALES+, SGDR-Ocean and SGDR-Seaice retracker for peaky waveforms in the Svalbard test area.

	ALES+	SGDR-Ocean	SGDR-Seaice
ERS-2	0.2620 m	0.3659 m	0.2901 m
Envisat	0.2142 m	0.2961 m	0.2364 m

results of the ocean retracker (more than 7 cm improvement for Envisat, more than 10 cm improvement for ERS-2), which is not able to fit peaky waveforms properly, but also of a dedicated solution (more than 2 cm improvement for Envisat against the sea ice retracker, 2.8 cm for ERS-2).

To further investigate the noise performances of ALES+ compared to a standard ocean retracker, the analysis of repetitive tracks in the open sea is needed. For this purpose, we limit our area of study using only the track segments that are out of the maximum extent of the sea ice, as shown in Figure 7. As a noise index we use the standard deviation of the high frequency data within a 1-Hz block. For comparison, the same analysis is performed using the SGDR ranges (from the ocean retracker) corrected and processed in the same way as ALES+ ranges. In the figure, the maps in (a) and (b) show for each 1-Hz point in ERS-2 and Envisat the median of the difference between the noise of the ocean retracker (SGDR) and the noise of the ALES+ retracker (ALES+). Positive numbers therefore mean that SGDR is noisier than ALES+. The histograms considering each 1-Hz point are shown in (c) and (d). In both missions, ALES+ is less noisy than SGDR in over 70% of the domain and in 20% of the domain it improves by over 3 cm. The maps show that, although the best improvements are reached at the border with the maximum sea ice extent, ALES+ is superior to the standard ocean retracking also in the open ocean. Overall, the median SGDR noise is 6.23 cm in Envisat and 9.18 cm in ERS-2, while the ALES+ noise is 5.08 cm in Envisat and 7.95 cm in ERS-2, meaning over 1.1 cm of improvement.

This demonstrates that the ALES+ compromise between a sufficient width of the subwaveform to characterise the signal. A limited influence of the noise in the trailing edge in the fitting allows a more precise estimation of the open ocean sea level, if compared with a full-waveform retracker. This clear improvement in the open ocean was not evident in Passaro et al. (2014) for ALES. The reason lies in the recomputation of the SSB correction using the ALES+ SWH and backscatter coefficient. We demonstrate this in Figure 9, where the standard deviation of the 1-Hz points is plotted against the SWH for ALES+ corrected by the standard SSB and by the recomputed SSB. For comparison, the SGDR statistics are also shown. From the linear fit it is evident that without a recomputed SSB correction ALES+ is slightly noisier than SGDR, while the new correction brings a strong improvement.

4.1.2. Comparison of sea level products

The main application of ALES+ is the provision of improved ranges that will be used to compute SLA in the SL CCI DTU/TUM high latitude sea level product. We evaluate the improvements in this section. We take RADS as an open ocean sea level reference that flags coastal and sea ice data, with the objective to show what improvements a dataset including these areas can bring to the sea level records.

We apply a gridding procedure to the dataset. First of all, outliers are treated by a MAD filter. The RADS data are per default already post-processed so no further outlier detection to this dataset is applied. Subsequently, for each week the SLA values are gridded using a least squares collocation (kriging) method with a second order Markov covariance function (Andersen, 1999):

$$c(r) = C_0 \left(1 + \frac{r}{\alpha}\right) e^{-r/\alpha} \tag{10}$$

where C_0 is the signal variance, r is the spatial distance, and α is the correlation length. The covariance scale is derived from the data variance, the correlation length is set to 500 km. Each grid cell measures 0.1° latitude × 0.5° longitude. For reference, we process RADS data in the same way. The collocation error is displayed in Figure 8 (a)-(b), while (c)-(f) show the number of valid measurements used for each grid point. The much higher number of measurements used by ALES+ is simply explained by the fact that it uses high-frequency measurements (18 Hz for Envisat, 20 Hz for ERS-2), while RADS is based on 1-Hz averages. This allows ALES+ to retrieve much more points in the sea ice-covered regions. Even if the number of measurements is much lower than in the open ocean, the error is kept below 2 cm also in most of the northern and coastal areas of the domain. Overall, the mean error for ALES+ in the sea ice covered zone is 2.1 cm (2.7 cm for RADS) while in the open ocean domain the mean error is 0.9 cm (1.3 cm for RADS).

Finally, we verify the accuracy of our sea level estimations by comparison with the Ny Ålesund TG. The location of the TG is visible in Figure 1(a). SLA from ALES+, generated from the range using the corrections in Section 3.3 is averaged in space in a radius of 350 km around the TG and in time to generate a monthly time series. The radius of 350 km is needed to perform a regional average that includes both sea ice cover and open ocean areas and the choice was already justified in the same area by Cheng et al. (2015). The agreement of the time series (Figure 10) is proved by a correlation of 0.85. For comparison, we also build a time series using RADS. Indeed, the better correlation using ALES+ is expected, given that RADS is not optimised for the Arctic Ocean: the benefit of the ALES+ retracking is particularly evident in the winter months of 1996 and 1998. As mentioned in Section 4.1, the winter of 1998 had the maximum sea ice extent; a significant part of the area considered for the comparison (the coast west of the Svalbard islands) was covered by sea ice and therefore the use of a standard altimetry product is more problematic. In the last decade, most of the area was ice-free during winter as well (not shown, see for example $https://nsidc.org/data/seaice_index/archives/image\_select.html$) and therefore the RADS and ALES+ time series are more similar.

4.2. Coast

In this Section, the performances of ALES+ in the coastal ocean are tested by comparison with the set of TGs in Figure 1 (b). The comparison is performed for detided time series of sea level. The amplitudes and phases of the tidal constituents in the tide gauge records were estimated on a year-by-year basis by harmonic analysis using the program t-tide (Pawlowicz et al., 2002). Harmonic analysis produces non-tidal residuals that are more representative of the true variability that can then be used as our ground truth against which we assess the altimetry data. Only constituents with a signal-to-noise ratio equal or larger than three were used to reconstruct the tidal signal. This guarantees the estimation of the most important constituents, while less energetic tidal constituents are not well resolved given the observations and their noise level and thus it is better to remove them.

At each tide gauge station, the performance of the altimetry data is assessed as a function of distance from the coast by assigning such data to distance bands of 1 km width starting from the 0-1 km band. As shown in Figure 1 (b), only data that fall within 70 km of the TG are used. For each altimetry pass we obtain one altimetry value by

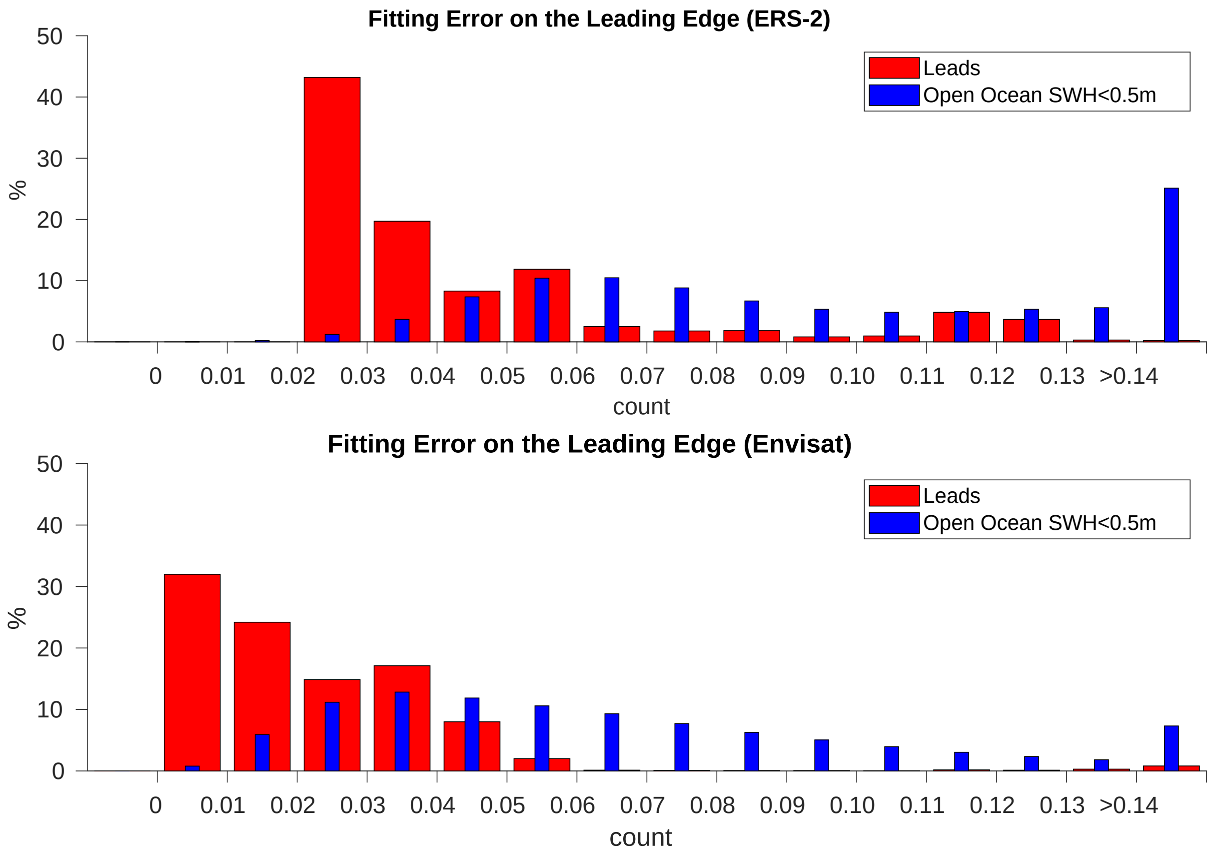

Figure 6: Error of the leading edge fit computed w.r.t. the normalised waveform for echoes classified as leads (red) and as open water with SWH<0.5 m (blue) in ERS-2 (upper plot) and Envisat (lower plot).

averaging all the high frequency records falling within the selected distance band. Records with an absolute SLA larger than 2 m or three standard deviations above the mean were rejected prior to computing the average. The corresponding tide gauge matching value is obtained by linearly interpolating the tide gauge observations to the time of the altimetry pass. The corresponding time series for each km-band are then evaluated according to the Percentage of Cycles for High Correlation (PCHC): the maximum percentage of cycles of data that could be retained while guaranteeing a correlation with the TG time series of at least 0.8 (Passaro et al., 2015b).The same procedure is applied to the SGDR ocean retracker and to the ALES retracker as described in Passaro et al. (2014), but with the addition of the recomputed SSB.

Firstly, the results are displayed in Figure 11 considering each TG-altimetry track couple. The values shown in the figures are the median PCHC in the last 10 km from the coast. Statistics vary considerably depending on the TG and satellite tracks. For

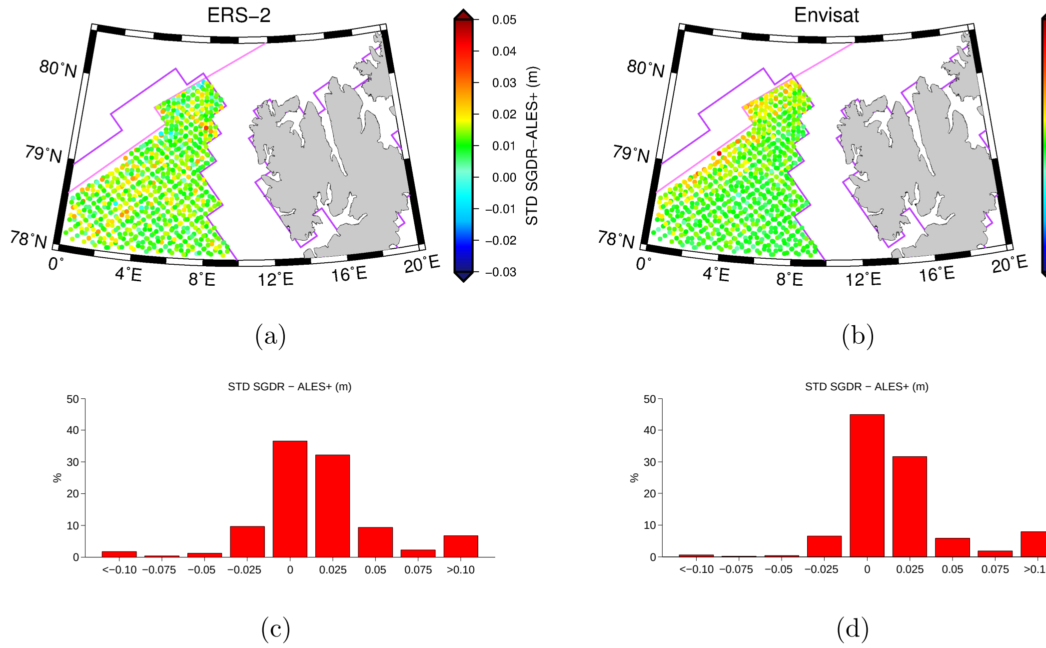

Figure 7: Difference of high-frequency noise in SGDR and ALES+ for ERS-2 (a,c) and Envisat (b,d). The noise is computed as standard deviation of the 1-Hz averages. The maps in (a) and (b) show the median of the noise difference for each 1-Hz point along the satellite tracks considering the entire period of study. Areas characterised by seasonal or multi-year sea ice are masked out.

example PCHC is below 20% in 2 cases for Envisat and 4 cases for ERS-2. This is partly related to the general worse performances and loss of altimetry data in land to sea transitions (see for example Gómez-Enri et al. (2016)). This is not a problem for our analysis, in which the objective is the comparison between the retrackers. In many cases, the three retrackers have very similar performances. This is well known from previous studies such as Passaro et al. (2014): a different retracking method is not always needed. Nevertheless, SGDR has a better PCHC than ALES+ in only 2 cases out of 33 in Envisat (Fishguard-401 and Workington-704) and ERS-2 (Fishguard-160 and Lowenstoff-57). In several cases ALES+ and ALES are substantially better than SGDR (for example Tregde-543 in ERS-2 and Wick-143 in Envisat). Nevertheless there are 3 cases in Envisat and 5 cases in ERS-2 in which ALES scores better than ALES+ by over 5%. To produce a final rating of the coastal performances with respect to the tide gauges, we looked at the median value of the PCHC considering all the tracks.

The results are displayed in Figure 12, where a median of the PCHC considering all 33 tracks is highlighted with a continuous line for each dataset. In terms of PCHC, the performances of the three retrackers are indistinguishable until 8 km from the coast. From 8 to 2 km from the coast, ALES is the best-performing dataset, followed by ALES+, while

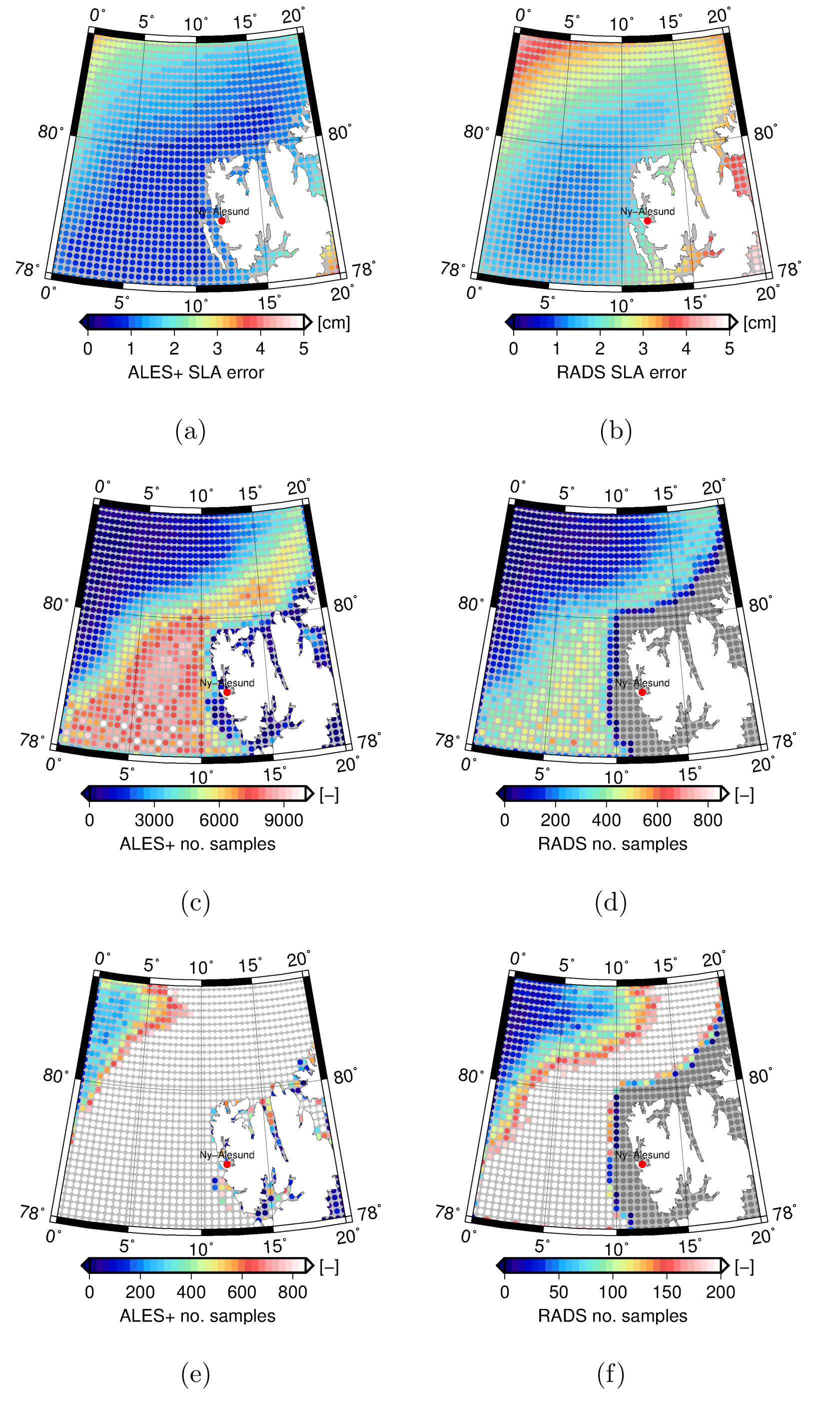

Figure 8: Collocation error estimate for (a) ALES+ and (b) RADS. The error is dependent on the number of samples. Number of samples in each grid cell for (c) ALES+ and (d) RADS. Notice the different color scales. (e) and (f) are the same as (c) and (d), but with saturated color scales in order to highlight points in the sea ice-covered areas.

SGDR is the worst-performing. In the last km, where waveforms are extremely irregular, but also where most of the oceanic peaky waveforms are located (Deng & Featherstone, 2006), ALES+ is the best performing dataset.

This is expected, since ALES+ needs to reach a compromise in the normalisation and leading edge detection, in order to be able to treat peaky waveforms as well, while the objective of ALES is to maximise the number of retracked coastal waveforms, which are normally characterised by strong peaks in the trailing edge.

We further validate and compare the retracking solutions by means of the comparison with the geoid model. The GOCO5s geoid height are interpolated to the altimetry tracks in the whole coastal area of the North Sea (Latitude limits: 50-61, Longitude limits: -11 15). We divide the domain via 5-km coastal distance bands. For each cycle of Envisat and ERS-2, after excluding unrealistic values of $|SLA| > 2$ m and $SWH > 11$m, we store the MAD of the differences between SSH and geoid height. Figure 13 show the averages of the results for Envisat and ERS-2. In the last 5 km to the coast, ALES scores better in terms of STD, and ALES+ scores second. Both are much better than the original SGDR data, which scores 2.7 cm worse than ALES+ for Envisat and 1.6 cm worse than ALES+ for ERS-2. ALES and ALES+ are of course equivalent going towards the open ocean and their MAD against the geoid is always lower than in SGDR.

We conclude that in the coastal zone ALES is the best choice among the three methods, but ALES+ scores constantly better than the current SGDR standard.

4.3. Inland waters

The possibility of using the same retracker to treat altimetry echoes from leads, open and coastal waters can be extended to retrieve water level in inland water bodies. Indeed, it has been shown that waveforms from rivers and small lakes are mostly quasi-specular or quasi-Brown (Berry et al., 2005).

For a first investigation, we have integrated the ALES+ ranges from Envisat for the Mekong river in the Database for Hydrological Time Series over Inland Waters (DAHITI, processed at the DGFI-TUM), in which altimetric ranges are used to produce water levels for river and lakes using a set of corrections, outlier rejection criteria and Kalman filter processing as described in Schwatke et al. (2015). As a comparison, we use the results from the Improved Threshold Retracker (ITR), implemented selecting a threshold of 50% (Hwang et al., 2006), processed through DAHITI in the same way as ALES+. The ITR is of common use in the reprocessing of inland water data (Hossain et al., 2014) and has already been used in the area of study (Boergens et al., 2016). It references a threshold value to the amplitude of the detected leading edge and determines the range by linearly interpolating between adjacent samples (Gommenginger et al., 2011).

The comparison of the water level time series is shown in Figure 14 and the results in terms of root mean square (RMS) error and correlation coefficient are reported in Table 2, as well as the number of points in each time series. It is observed that none of the retrackers is able to catch the water extremes: this is due to the fact that the temporal resolution of Envisat (one pass every 35 days) is suboptimal compared to an in-situ gauge. The results of the two retrackers are comparable in terms of correlation, while ITR has a better RMS in two of the three stations. In Kratie, if one excludes the clear outlier in the time series in 2003, ALES+ RMS scores 1.37 and therefore is inline with the ITR result. Also the number of points in the time series is comparable between both retrackers in two of the three stations, while only in Mukdahan ITR has considerably more points. Unfortunately, the comparison with the gauges is only relative, because the in-situ stations lack an absolute reference. Nevertheless, the average bias between ALES+ and ITR changes from 1.8 m in Luang Prabang to slightly more than 0.30 m in Mukdahan and Kratie. The variable bias is due to the fact that, while ITR locates the range using always the same threshold of the waveform amplitude, the location of the retracking point of ALES+ varies depending on the estimated c_ξ, as explained in Section 3.1.1. Further validation against absolute water levels are needed to assess whether this improves the accuracy of the altimeter for rivers.

Table 2: Comparison of water level time series in the Mekong river from Envisat retracked by ALES+ and by Improved Threshold Retracker at 50% w.r.t. data from three TGs. In terms of root mean square (RMS), correlation coefficient and number of points in the time series (Num of points).

		RMS (m)	Correlation Coefficient	Num of points
Luang Prabang vs Envisat pass 651	ALES+	0.87	0.97	72
	ITR 50%	0.81	0.97	72
Mukdahan vs Envisat pass 21	ALES+	0.79	0.99	69
	ITR 50%	0.79	0.99	74
Kratie vs Envisat pass 565	ALES+	1.59	0.96	80
	ITR 50%	1.33	0.98	79

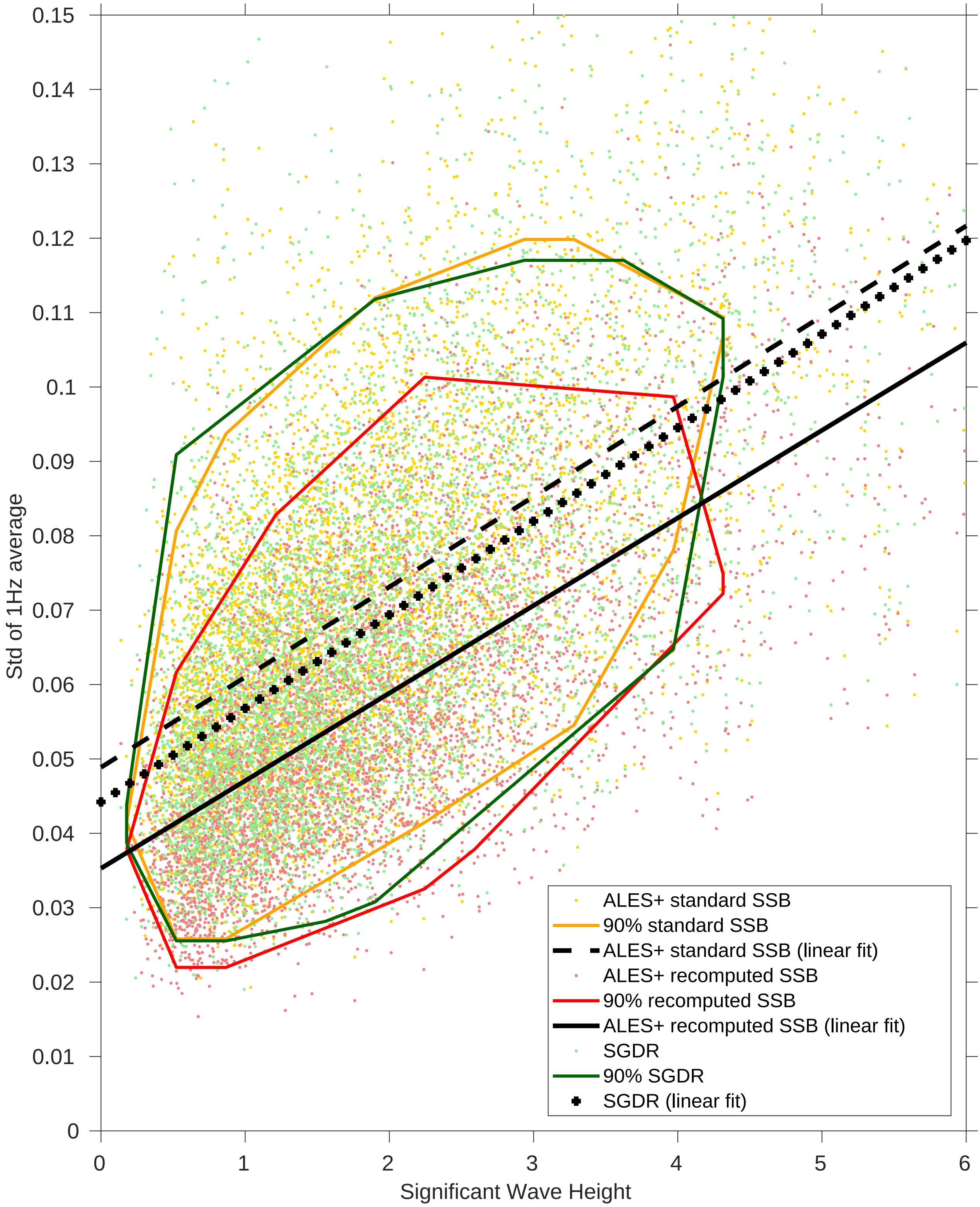

Figure 9: Scatter plot and linear fit of the standard deviations of the 1-Hz points (used as measurement of high-frequency noise) against the SWH, for ALES+ corrected by the standard SSB and by the recomputed SSB. For comparison, the SGDR statistics are also shown. The contours delimit the location of 90% of the data for each dataset.

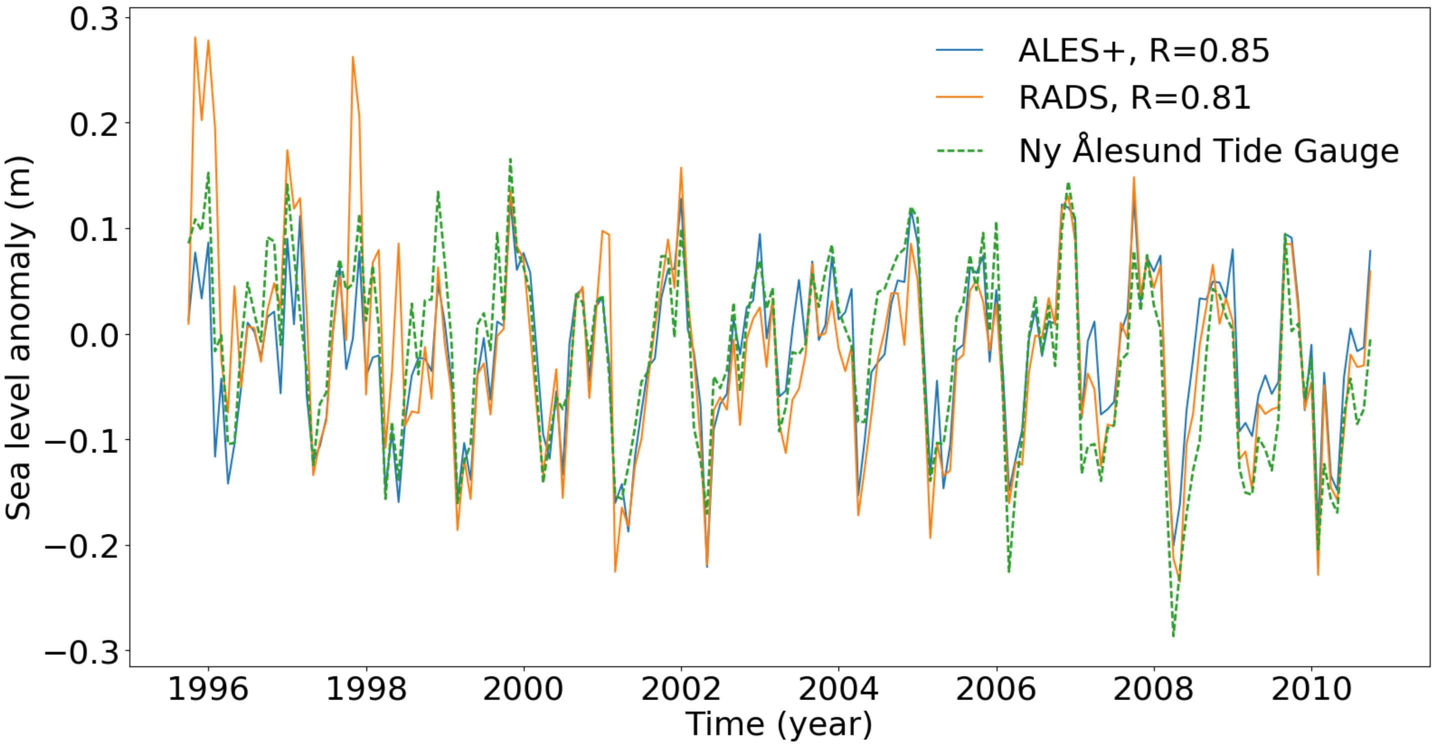

Figure 10: Time series of SLA of ALES+ and RADS data compared to the Ny Alesund TG. The gridded weekly median data are resampled to monthly SLAs. The inverse barometer effect is excluded to be comparable to the TG. R stands for the value of the correlation coefficient between the corresponding altimetry dataset and the TG.

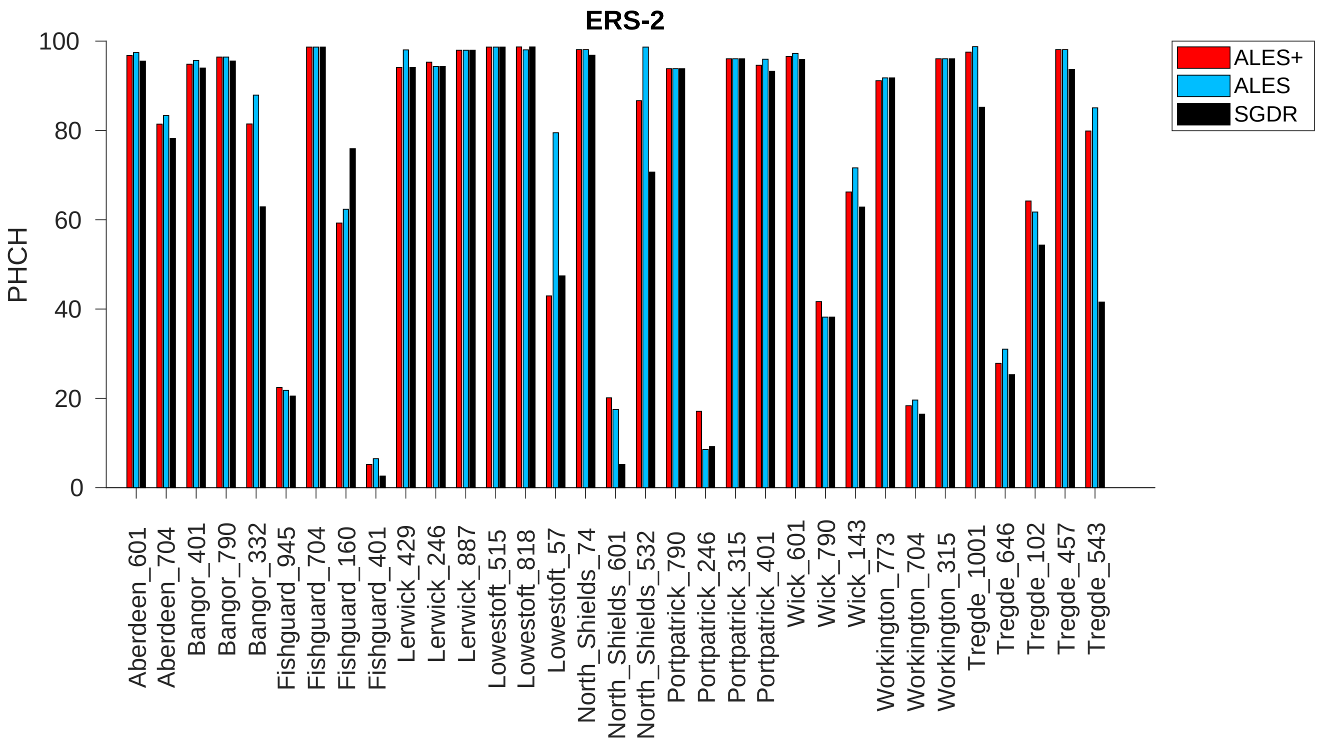

(a)

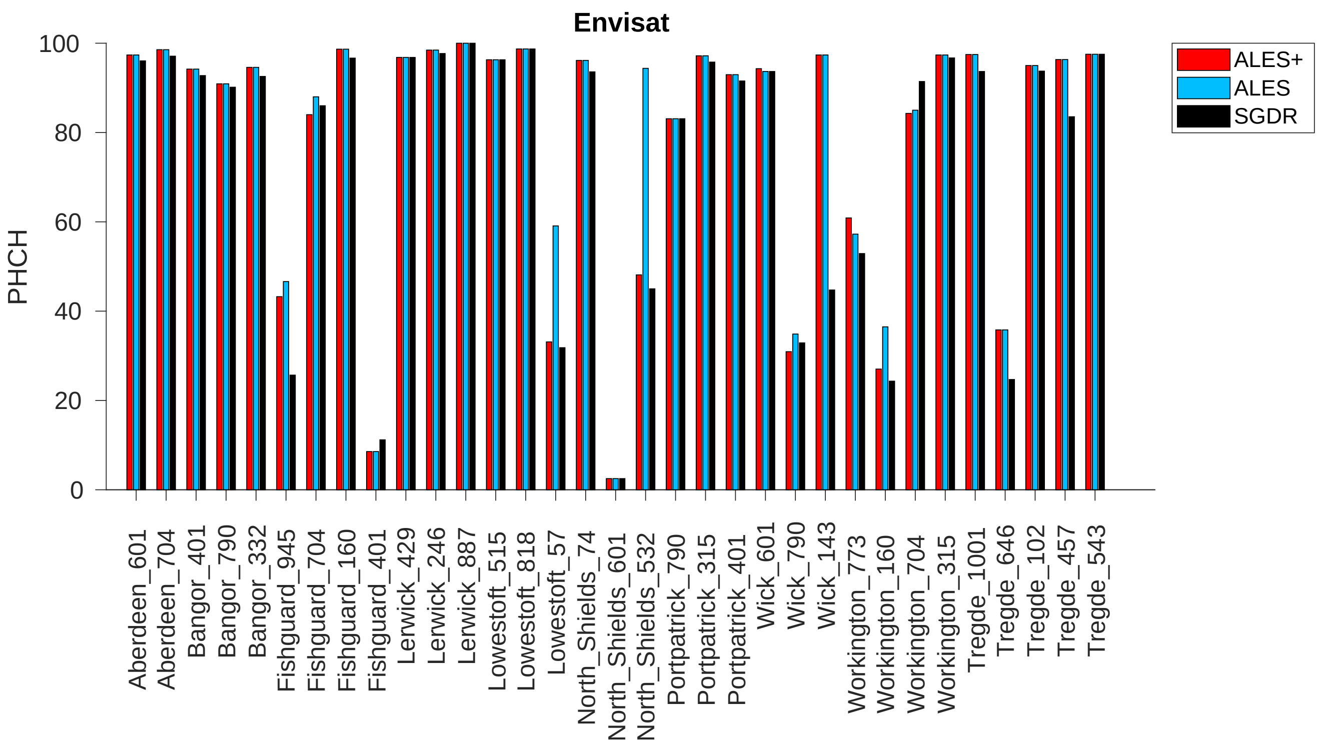

(b)

Figure 11: Median PCHC for ERS-2 tracks (upper plot) and the Envisat tracks (lower plot) within 10 km of the TG for SGDR, ALES+ and ALES (with recomputed SSB). On the x axis, the name of each TG and the corresponding satellite track numbers are shown.

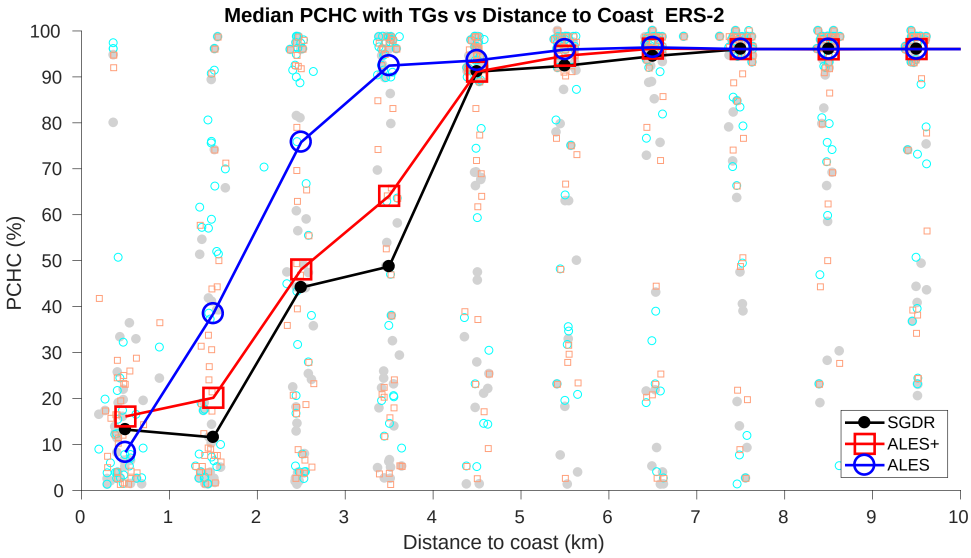

(a)

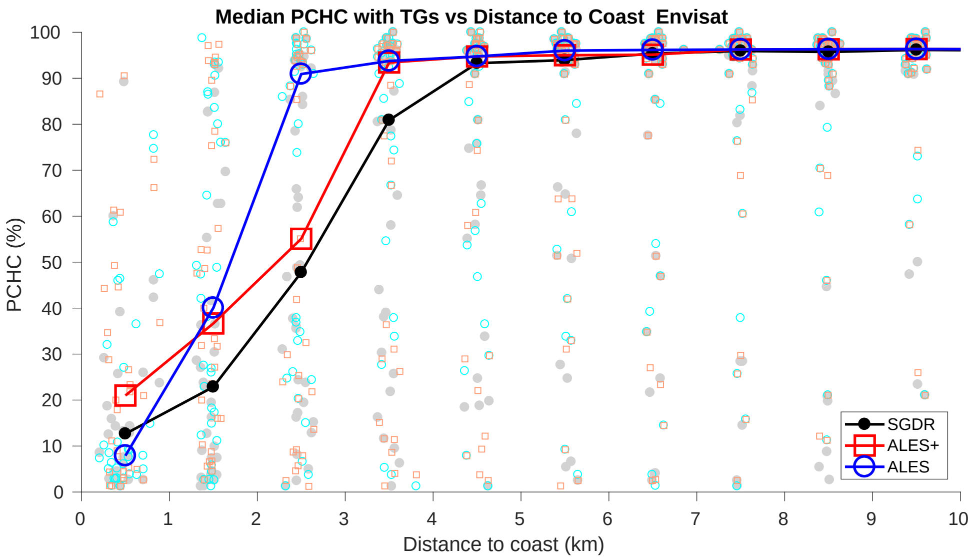

(b)

Figure 12: PCHC for ERS-2 tracks (upper plot) and the Envisat tracks (lower plot) within 10 km of the TG w.r.t. the distance to the coast for SGDR, ALES+ and ALES (with recomputed SSB). Single results are shown as grey dots (SGDR), red squares (ALES+) and cyan circles (SGDR). The continuous lines show the median of the statistics.

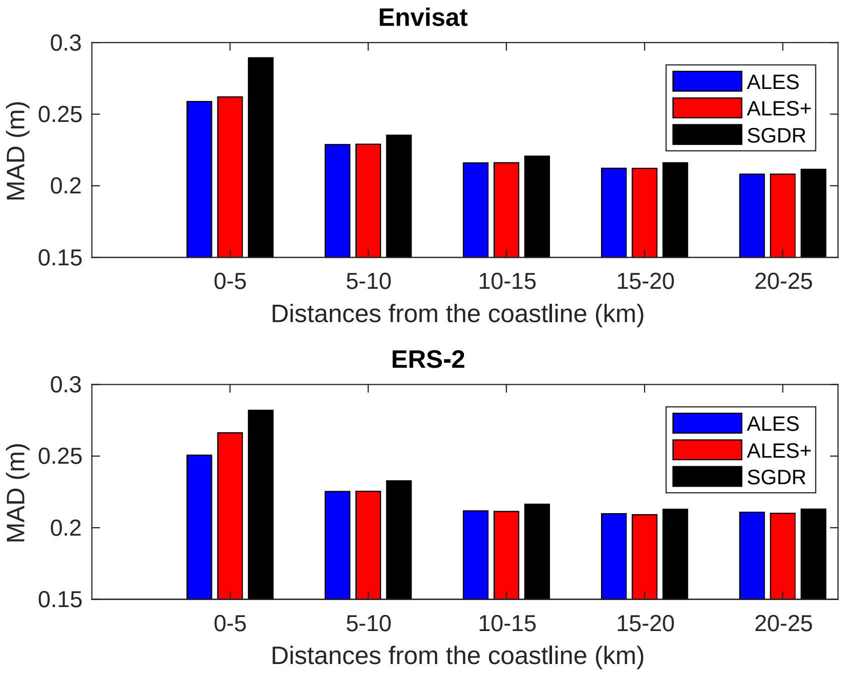

Figure 13: Median Absolute Deviation between GOCO5s geoid heights and SSH data retracked with ALES, ALES+ and SGDR in 5-km wide distance bands.

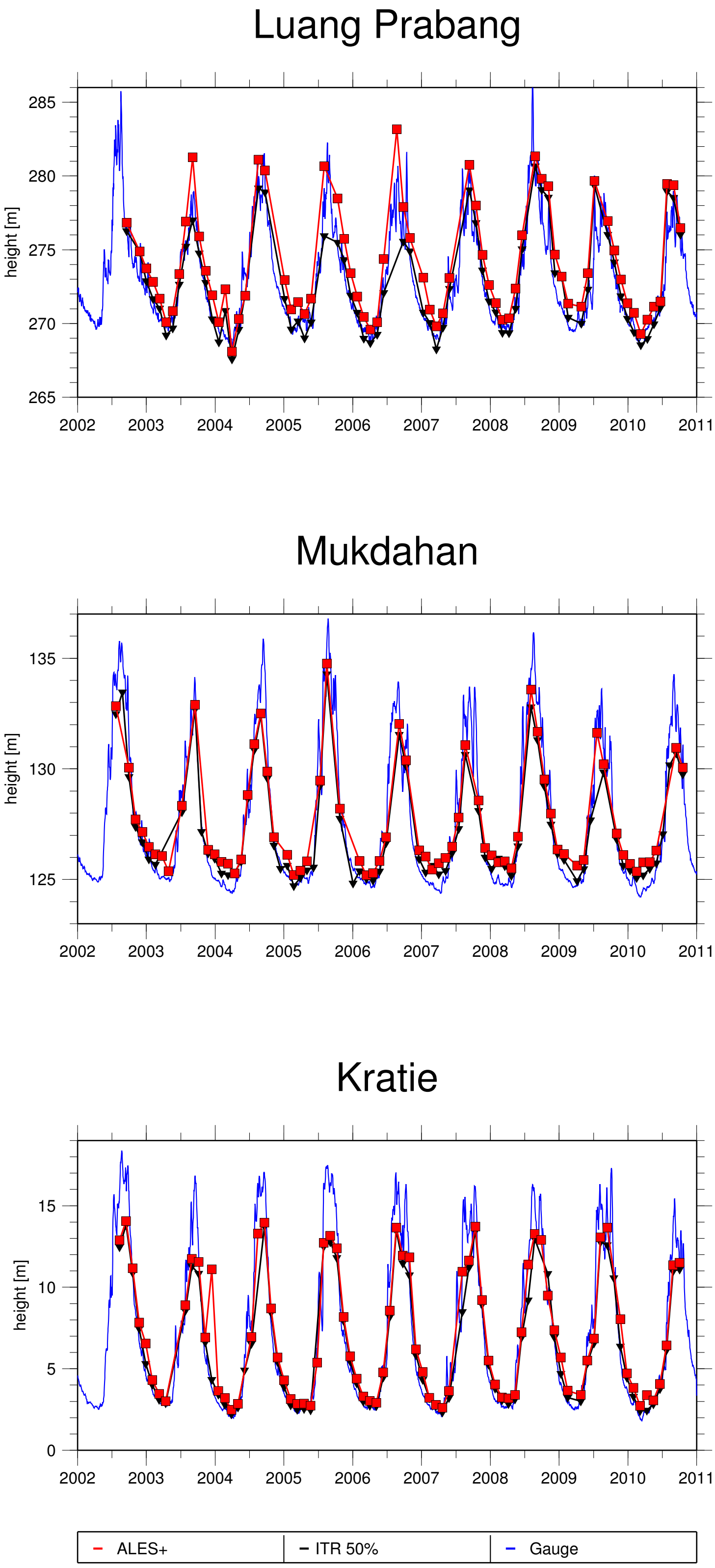

Figure 14: Visual comparison of water level time series in the Mekong river from Envisat retracked by ALES+ (red squares), Envisat retracked by Improved Threshold Retracker at 50% and data from three gauges.

5. Conclusion

In this study, we have presented a homogenous retracking strategy that uses the same functional form to fit signals reflected back from leads in the sea ice pack and open ocean. The algorithm named ALES+ is applied to ERS-2 and Envisat missions and is based on modifications to the ALES algorithm described in Passaro et al. (2014). Thanks to a preliminary step aimed at estimating the slope of the trailing edge, it is able to adapt the fitting to specular echoes. As a result of a subwaveform strategy aimed at limiting the impact of the noise in the trailing edge and to a recomputed SSB correction, it is able to decrease the high-frequency noise by over 1.1 cm in the open sea unaffected by sea ice. Even considering only peaky waveforms, range retrieval by ALES+ is over 2 cm more precise than the available solution used in previous studies to estimate sea level from leads (the sea ice retracker).

The validation against a TG situated on the Svalbard islands demonstrates that ALES+ can improve the quality and the amount of data of the sea level records at high-latitudes. The improvement is brought by the retracking of non-standard ocean waveforms and the use of high-frequency data instead of 1-Hz averages, which are of limited use at high-latitudes given that most of the leads are narrower than 1 km (Lindsay & Rothrock, 1995; Kwok et al., 2009). ALES+ is able to decrease the error on the sea level estimation of the sea ice-covered ocean up to a comparable level with the open ocean and therefore should be used in the next steps of the research to update the sea level record in the Arctic and Antarctic ocean.

The lower noise of ALES+ in the open ocean could be used to study mesoscale structures and a spectral analysis should be able to reveal if this can be useful to solve at least partially the noise problems that affect standard altimetry at these scales (Dibarboure et al., 2014). The improvements obtained by recomputing the SSB using ALES+ estimations could be even higher if a new SSB model is recomputed specifically for this retracker.

A validation against coastal TGs has demonstrated that ALES+ improves the quality of sea level retrievals in the last 6 km within the coastline compared to the standard open ocean retracking. For coastal studies, ALES still overperforms ALES+. As a possible improvement to ALES+, future studies will seek a better strategy for the leading edge detection in order to avoid that peaks in the trailing edge, typical of coastal waveforms, could be interpreted as peaky leading edges by the algorithm.

A preliminary validation has shown that ALES+ time series of water level of the Mekong River are very highly correlated with in-situ data. Nevertheless, the typical retracker used for inland waters (improved threshold) have better statistics, mainly due to outliers still present in ALES+. Future studies should further validate this application and exploit the seamless transition between inland waters and open sea, in order to study the sea level variations across deltas and estuaries.

In conclusion, ALES+ offers the chance to fit the echoes from any water surface without the need to change the retracking strategy and therefore avoiding internal bias corrections and calibrations. It provides a more precise and accurate sea level estimation than the available sea ice and ocean retrackers for ERS-2 and Envisat in leads and in open and coastal waters.

Acknowledgements

The authors acknowledge the support of the European Space Agency in the framework of the Sea Level Climate Change Initiative project.

The first author is thankful to Christian Schwatke for the help in storing the altimetry data, Paolo Cipollini, Jesus Gomez-Enri, Graham Quartly and Pierre Thibaut for the discussions on the development of the algorithm, and to David Sestak for the help with the Generic Mapping Tools software.

The authors would like to thank the anonymous reviewers for their valuable comments and suggestions aimed at improving the quality of the paper.

Bibliography

Abdalla, S. (2012). Ku-band radar altimeter surface wind speed algorithm. *Marine Geodesy*, *35*, 276–298. http://doi.org/10.1080/01490419.2012.718676.

Ablain, M., Legeais, J., Prandi, P., Marcos, M., Fenoglio-Marc, L., Dieng, H., Benveniste, J., & Cazenave, A. (2016). Satellite altimetry-based sea level at global and regional scales. *Surveys in Geophysics*, (pp. 1–25). http://doi.org/10.1007/s10712-016-9389-8.

Akima, H. (1970). A new method of interpolation and smooth curve fitting based on local procedures. *Journal of the ACM*, *17*, 589–602. http://doi.org/10.1145/321607.321609.

Andersen, O. B. (1999). Shallow water tides in the northwest european shelf region from TOPEX/POSEIDON altimetry. *Journal of Geophysical Research-Oceans*, *104*, 7729–7741. http://doi.org/10.1080/01490419.2012.718676.

Andersen, O. B., Stenseng, L., Piccioni, G., & Knudsen, P. (presented at the ESA Living Planet Symposium 2016). The DTU15 MSS (Mean Sea Surface) and DTU15LAT (Lowest Astronomical Tide) reference surface.

Berry, P., Garlick, J., Freeman, J., & Mathers, E. (2005). Global inland water monitoring from multi-mission altimetry. *Geophysical Research Letters*, *32*. http://doi.org/10.1029/2005GL022814.

Boergens, E., Dettmering, D., Schwatke, C., & Seitz, F. (2016). Treating the hooking effect in satellite altimetry data: A case study along the mekong river and its tributaries. *Remote Sensing*, *8*, 91. http://doi.org/10.3390/rs8020091.

Brown, G.S. (1977). The average impulse response of a rough surface and its applications. *IEEE Transaction on Antennas and Propagation*, *25*, 67–74. https://doi.org/10.1109/TAP.1977.1141536

Carrere, L., Lyard, F., Cancet, M., & Guillot, A. (2015). Fes 2014, a new tidal model on the global ocean with enhanced accuracy in shallow seas and in the arctic region. In *EGU General Assembly Conference Abstracts* (p. 5481). volume 17.

Cazenave, A., Dieng, H.-B., Meyssignac, B., von Schuckmann, K., Decharme, B., & Berthier, E. (2014). The rate of sea-level rise. *Nature Clim. Change*, *4*, 358–361. http://doi.org/10.1038/nclimate2159

Chelton, D. B., & McCabe, P. J. (1985). A review of satellite altimeter measurement of sea surface wind speed: With a proposed new algorithm. *Journal of Geophysical Research*, *90*, 4707. http://doi.org/10.1029/JC090iC03p0470.

Cheng, Y., Andersen, O., & Knudsen, P. (2015). An improved 20-year arctic ocean altimetric sea level data record. *Marine Geodesy*, *38*, 146–162. http://doi.org/10.1080/01490419.2014.954087

Cipollini, P., Calafat, F. M., Jevrejeva, S., Melet, A., & Prandi, P. (2017). Monitoring sea level in the coastal zone with satellite altimetry and tide gauges. *Surveys in Geophysics*, (pp. 1–25). http://doi.org/10.1007/s10712-016-9392-0.

Dibarboure, G., Boy, F., Desjonqueres, J., Labroue, S., Lasne, Y., Picot, N., Poisson, J., & Thibaut, P. (2014). *Journal of Atmospheric and Oceanic Technology*, *31(6)*, 1337–1362. http://doi.org/doi.org/10.1175/JTECH-D-13-00081.1

Deng, X., & Featherstone, W. (2006). A coastal retracking system for satellite radar altimeter waveforms: application to ERS-2 around Australia. *Journal of Geophysical Research-Space*, *111*, C06012. http://doi.org/10.1029/2005JC003039

Dorandeu, J., Ablain, M., Faugere, Y., Mertz, F., Soussi, B., & Vincent, P. (2004). Jason-1 global statistical evaluation and performance assessment: Calibration and cross-calibration results. *Marine Geodesy*, *27*, 345–372. http://doi.org/10.1080/01490410490889094

Drinkwater, M. R. (1991). Ku Band Airborne Radar Altimeter Observations of Marginal Sea Ice During the 1984 Marginal Ice Zone Experiment. *Journal of Geophysical Research*, *96*, 4555–4572. http://doi.org/10.1080/01490410490889094

Femenias, P., Baker, S., Brockley, D., Martinez, B., Massmann, F. H., Otten, M., Picard, B., Roca, M., Rudenko, S., Scharroo, R., Soulat, F., Visser, P., Paul, F., & Fische, P. (2014). Reprocessing of the ERS-1 and ERS-2 altimetry missions. the REAPER project. *presented at the Ocean Surface Topography Science Team meeting, Konstanz, Germany*, . http://doi.org/10.13140/2.1.3756.7685.

Fetterer, F. M., Drinkwater, M. R., Jezek, K. C., Laxon, S. W., & Onstott, R. G. (1992). Sea ice altimetry. In F. D. Carsey (Ed.), *Microwave remote sensing of sea ice*. DTIC Document. http://doi.org/10.1029/GM068p0111

Fertterer, F. Knowles, K. Meier, W. Savoie, M. (2016). Sea Ice Index. *NSIDC: National Snow and Ice Data Center*, http://doi.org/10.7265/N5736NV7.

Fu, L., & Cazenave, A. (Eds.) (2001). *Satellite altimetry and earth sciences. A handbook of techniques and applications.* volume 69. San Diego, CA: Academic.

Gilbert, L., Baker, S., Dolding, C., Vernier, A., Brockley, D., Martinez, B., & Gaudelli, J. (2014). Reaper: Product handbook for ers altimeters reprocessed products v. 3.1. *ESA User Manual, ESA*, .

Giles, K. A., Laxon, S. W., Wingham, D. J., Wallis, D. W., Krabill, W. B., Leuschen, C. J., McAdoo, D., Manizade, S. S., & Raney, R. K. (2007). Combined airborne laser and radar altimeter measurements over the Fram Strait in May 2002. *Remote Sensing of Environment*, *111*, 182–194. http://doi.org/10.1016/j.rse.2007.02.037

Gómez-Enri, J., Cipollini, P., Passaro, M., Vignudelli, S., Tejedor, B., & Coca, J. (2016). Coastal altimetry products in the Strait of Gibraltar. *IEEE Transactions on Geoscience and Remote Sensing*, *54*, 5455 – 5466. http://doi.org/10.1038/ngeo1379

Gommenginger, C., Thibaut, P., Fenoglio-Marc, L., Quartly, G. D., Deng, X., Gómez-Enri, J., Challenor, P. G., & Gao, Y. (2011). Retracking altimeter waveforms near the coasts. In S. Vignudelli, A. Kostianoy, P. Cipollini, & J. Benveniste (Eds.), *Coastal Altimetry* (pp. 61–102). Berlin Heidelberg: Springer-Verlag. https://doi.org/10.1007/978-3-642-12796-0_4

Handoko, E. Y., Fernandes, M. J., & Lzaro, C. (2017). Assessment of altimetric range and geophysical corrections and mean sea surface modelsimpacts on sea level variability around the indonesian seas. *Remote Sensing*, *9*. http://doi.org/10.3390/rs9020102.

Hayne, G. S. (1980). Radar altimeter mean return waveforms from near-normal-incidence ocean surface scattering. *IEEE Transaction on Antennas and Propagation*, *28*, 687–692. https://doi.org/10.1109/TAP.1980.1142398

Hossain, F., Siddique-E-Akbor, A., Mazumder, L. C., ShahNewaz, S. M., Biancamaria, S., Lee, H., & Shum, C. (2014). Proof of concept of an altimeter-based river forecasting system for transboundary flow inside Bangladesh. *IEEE Journal of Selected Topics in Applied Earth Observations and Remote Sensing*, *7*, 587–601.https://doi.org/10.1109/JSTARS.2013.2283402

Hwang, C., Guo, J., Deng, X., Hsu, H.-Y., & Liu, Y. (2006). Coastal gravity anomalies from retracked Geosat/GM altimetry: Improvement, limitation and the role of airborne gravity data. *Journal of Geodesy*, *80*, 204–216. https://doi.org/10.1007/s00190-006-0052-x

Jackson, F., Walton, W., Hines, D., Walter, B., & Peng, C. (1992). Sea surface mean square slope from Ku-band backscatter data. *Journal of Geophysical Research: Oceans*, *97*, 11411–11427. http://dx.doi.org/10.1029/92JC00766

Kwok, R., Cunningham, G., Wensnahan, M., Rigor, I., Zwally, H., & Yi, D. (2009). Thinning and volume loss of the Arctic Ocean sea ice cover: 2003–2008. *Journal of Geophysical Research: Oceans*, *114*. http://doi.org/10.1029/2009JC005312

Labroue, S. (2007). *RA2 Ocean and MWR Measurement Long Term Monitoring, 2007 Report for WP3, Task 2SSB Estimation for RA2 Altimeter*. Technical Report Contract 17293/03/I-OL, CLS-DOS-NT-07-198, CLS, Ramonville St. Agne, France. URL: ftp://ftp.esa-sealevel-cci.org/Data/TechnicalRef/PhaseE_envisat_ssb_report_2010.pdf.

Laxon, S. (1994a). Sea ice extent mapping using the ERS-1 radar altimeter. *EARSeL Advances in Remote Sensing*, *3*, 112–116. URL: http://www.earsel.org/Advances/3-2-1994/3-2_13_Laxon.pdf.

Laxon, S. W. (1994b). Sea ice altimeter processing sheme at the EODC. *International Journal of Remote Sensing*, *15*, 915–924. https://doi.org/10.1080/01431169408954124

Lindsay, R., & Rothrock, D. (1995). Arctic sea ice leads from advanced very high resolution radiometer images. *Journal of Geophysical Research: Oceans*, *100*, 4533–4544. https://doi.org/10.1080/01431169408954124

Marshall, J., Armour, K. C., Scott, J. R., Kostov, Y., Hausmann, U., Ferreira, D., Shepherd, T. G., & Bitz, C. M. (2014). The ocean's role in polar climate change: asymmetric arctic and antarctic responses to greenhouse gas and ozone forcing. *Philosophical Transactions of the Royal Society of London A: Mathematical, Physical and Engineering Sciences*, *372*, 20130040. https://doi.org/10.1098/rsta.2013.0040

Neumann, B., Vafeidis, A. T., Zimmermann, J., & Nicholls, R. J. (2015). Future coastal population growth and exposure to sea-level rise and coastal flooding-a global assessment. *PloS one*, *10*, e0118571. https://doi.org/10.1371/journal.pone.0118571

Pail, R., Goiginger, H., Schuh, W.-D., Hoeck, E. , Brockmann, J.M., Fecher, T., Gruber, T., Mayer-Guerr, T., Kusche, J., Jaeggi, A. & Rieser, D. (2010). Combined satellite gravity field model GOCO01S derived from GOCE and GRACE. *Geophysical Research Letters*, *37*, L20314. https://10.1029/2010GL044906

Palanisamy, H., Cazenave, A., Delcroix, T., & Meyssignac, B. (2015). Spatial trend patterns in the pacific ocean sea level during the altimetry era: The contribution of thermocline depth change and internal climate variability. *Ocean Dynamics*, (pp. 1–16).

Pascual, A., Faugère, Y., Larnicol, G., & Le Traon, P.-Y. (2006). Improved description of the ocean mesoscale variability by combining four satellite altimeters. *Geophysical Research Letters*, *33*, L02611. http://doi.org/10.1029/2005GL024633

Passaro, M., Cipollini, P., & Benveniste, J. (2015a). Annual sea level variability of the coastal ocean: The Baltic Sea-North Sea transition zone. *Journal of Geophysical Research: Oceans*, *120*, 3061–3078. http://doi.org/10.1002/2014JC010510

Passaro, M., Cipollini, P., Vignudelli, S., Quartly, G., & Snaith, H. (2014). ALES: A multi-mission subwaveform retracker for coastal and open ocean altimetry. *Remote Sensing of the Environment*, *145*, 173–189. http://doi.org/10.1016/j.rse.2014.02.008.

Passaro, M., Dinardo, S., Quartly, G. D., Snaith, H. M., Benveniste, J., Cipollini, P., & Lucas, B. (2016). Cross-calibrating ALES Envisat and Cryosat-2 Delay–Doppler: A coastal altimetry study in the Indonesian Seas. *Advances in Space Research*, *58*, 289303.

Passaro, M., Fenoglio-Marc, L., & Cipollini, P. (2015b). Validation of significant wave height from improved satellite altimetry in the German Bight. *IEEE Transactions on Geoscience and Remote Sensing*, *53*, 2146–2156. http://doi.org/10.1109/TGRS.2014.2356331.

Passaro, M., Mueller, F.L., & Dettmering, D. (2017). Lead detection using Cryosat-2 delay-doppler processing and Sentinel-1 SAR images. *Advances in Space Research*. http://doi.org/10.1016/j.asr.2017.07.011

Pawlowicz, R., Beardsley, B., & Lentz, S. (2002). Classical tidal harmonic analysis including error estimates in matlab using t_tide. *Computers & Geosciences*, *28*, 929–937. http://doi.org/10.1016/j.asr.2017.07.011

Peacock, N. R., & Laxon, S. W. (2004). Sea surface height determination in the Arctic ocean from ERS altimetry. *Journal of Geophysical Research: Oceans*, *109*. http://doi.org/10.1029/2001JC001026

Poisson, J., Quartly, G. D., Kurekin, A., Thibaut, P., Hoang, D., & Nencioli, F. (2017). Extending sea level estimation into the Arctic Ocean using ENVISAT altimetry. *submitted to IEEE Transactions on Geoscience and Remote Sensing* .

Quartly, G. D., Srokosz, M. A., & McMillan, A. C. (2001). Analyzing altimeter artifacts: Statistical properties of ocean waveforms. *Journal of Atmospheric and Oceanic Technology*, *18*, 2074–2091. https://doi.org/10.1175/1520-0426(2001)018<2074:AAASPO>2.0.CO;2

Rose, S., Passaro, M., & Andersen, O. (in preparation). A 25 year Arctic Ocean sea level record for the Climate Change Initiative project .

Rudenko, S., Dettmering, D., Esselborn, S., Schöne, T., Förste, C., Lemoine, J.-M., Ablain, M., Alexandre, D., & Neumayer, K.-H. (2014). Influence of time variable geopotential models on precise orbits of altimetry satellites, global and regional mean sea level trends. *Advances in Space Research*, *54*, 92–118. https://doi.org/10.1016/j.asr.2014.03.010

Savcenko, R., & Bosch, W. (2012). *EOT11a - Empirical Ocean Tide Model From Multi-Mission Satellite Altimetry*. Technical Report DGFI No. 89. URL: https://epic.awi.de/36001/1/DGFI_Report_89.pdf.

Sandwell, D.T., & Smith, W.H.F. (2005). Retracking ERS-1 altimeter waveforms for optimal gravity field recovery. *Geophysical Journal International*, *163*, 79–89. http://doi.org/10.1111/j.1365-246X.2005.02724.x

Schwatke, C., Dettmering, D., Bosch, W., & Seitz, F. (2015). DAHITI–an innovative approach for estimating water level time series over inland waters using multi-mission satellite altimetry. *Hydrology and Earth System Sciences*, *19*, 4345–4364. https://doi.org/10.5194/hess-19-4345-2015

Stammer, D., Ray, R., Andersen, O., Arbic, B., Bosch, W., Carrère, L., Cheng, Y., Chinn, D., Dushaw, B., Egbert, G. et al. (2014). Accuracy assessment of global barotropic ocean tide models. *Reviews of Geophysics*, . http://doi.org/10.1002/2014RG000450.

Vinogradov, S., & Ponte, R. (2010). Annual cycle in coastal sea level from tide gauges and altimetry. *Journal of Geophysical Research: Space*, *115*, C04021. http://doi.org/10.1029/2009JC005767